Chemical Science

ROYAL SOCIETY OF CHEMISTRY

REVIEW

View Article Online
View Journal | View Issue

Cite this: *Chem. Sci.*, 2024, **15**, 6285

Emerging single-atom catalysts in the detection and purification of contaminated gases

Lingyue Liu,[a] Ka-Fu Yung,*[a] Hongbin Yang*[b] and Bin Liu *[cd]

Single atom catalysts (SACs) show exceptional molecular adsorption and electron transfer capabilities owing to their remarkable atomic efficiency and tunable electronic structure, thereby providing promising solutions for diverse important processes including photocatalysis, electrocatalysis, thermal catalysis, *etc.* Consequently, SACs hold great potential in the detection and degradation of pollutants present in contaminated gases. Over the past few years, SACs have made remarkable achievements in the field of contaminated gas detection and purification. In this review, we first provide a concise introduction to the significance and urgency of gas detection and pollutant purification, followed by a comprehensive overview of the structural feature identification methods for SACs. Subsequently, we systematically summarize the three key properties of SACs for detecting contaminated gases and discuss the research progress made in utilizing SACs to purify polluted gases. Finally, we analyze the enhancement mechanism and advantages of SACs in polluted gas detection and purification, and propose strategies to address challenges and expedite the development of SACs in polluted gas detection and purification.

Received 14th February 2024
Accepted 1st April 2024

DOI: 10.1039/d4sc01030b

rsc.li/chemical-science

1. Introduction

The emission of pollutants such as sulfur oxides (SO_x), nitrogen oxides (NO_x), carbon oxides (CO_x), and volatile organic compounds (VOCs) from activities and industrial manufacturing processes of human beings poses a substantial risk to human health, leading to emergence of various diseases, disruption of ecological balance, and decline in biodiversity.[1–4] The real-time detection and purification of contaminated gases are therefore of paramount importance and merit significant attention.[5] The monitoring and purification processes both involve adsorption and activation of contaminated gas molecules, highlighting the pivotal role of catalysis in contaminated gas detection and purification. Therefore, a profound comprehension of catalytic mechanisms in gas detection and purification processes is indispensable for the development of cutting-edge catalysts.

Single atom catalysts (SACs) demonstrate maximum atom utilization efficiency with tunable electronic structure through manipulating the single atom centers, coordination atoms and/or coordination numbers.[6–12] Moreover, SACs offer an ideal platform to investigate the structure–performance relationship thanks to their homogeneous isolated active centers.[13–16] Most gas sensors operate based on catalytic processes, making SACs ideal for high-performance gas sensing applications.[17,18] Early research showed that compared to traditional gas sensing materials, SACs could maintain high sensitivity and rapid response even at low temperatures.[19–22] The efficient catalytic activity of metal single atoms and their synergistic effects with metal supports play crucial roles in this context.[23–25] Over the past decades, various strategies have been employed to control emissions of contaminated gases, including absorption, condensation, biological degradation, and catalysis. Among these approaches, catalysis shows great promise in eliminating contaminated gases, advancing clean energy development, and producing high-value chemicals. Thus, it is crucial to design and develop highly efficient and chemically stable heterogeneous catalysts with adjustable structures and abundant active sites to address challenges associated with contaminated gas detection and purification.[26,27] SACs have demonstrated exceptional performance in purifying contaminated gas by converting it into harmless products and even value-added fuels/chemicals.[28,29] Understanding the scientific mechanisms of SACs in this field will greatly contribute to advancing their applications in gas sensing and gas purification.[30,31]

In this review, the characterization methods to determine the structure of SACs is first outlined. Next, the working mechanisms of gas sensors are systematically summarized, followed by a comprehensive description of research progress in

[a]*Department of Applied Biology and Chemical Technology, The Hong Kong Polytechnic University, Hung Hom, Kowloon, Hong Kong, China. E-mail: kf.yung@polyu.edu.hk*

[b]*School of Materials Science and Engineering, Suzhou University of Science and Technology, Suzhou 215009, China. E-mail: yanghb@usts.edu.cn*

[c]*Department of Materials Science and Engineering, City University of Hong Kong, Tat Chee Avenue, Kowloon, Hong Kong SAR 999007, China. E-mail: bliu48@cityu.edu.hk*

[d]*Department of Chemistry, Hong Kong Institute of Clean Energy & Center of Super-Diamond and Advanced Films (COSDAF), City University of Hong Kong, Hong Kong SAR 999077, China*

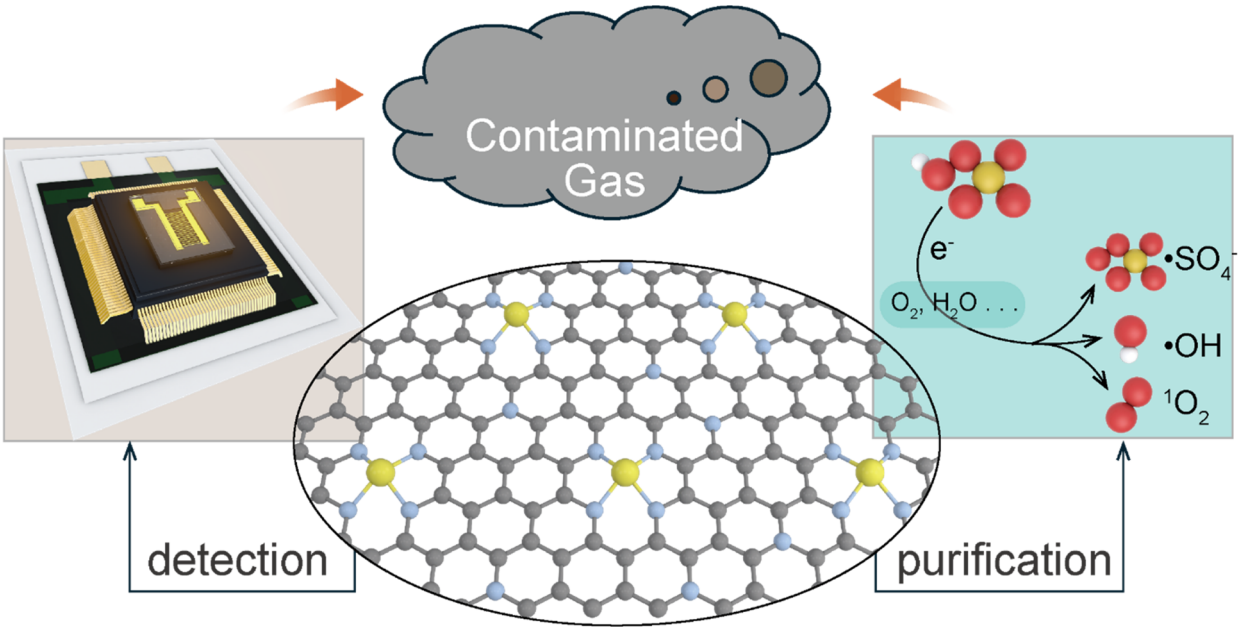

Scheme 1 A comprehensive summary diagram illustrating the overview of the manuscript.

gas sensing using SACs, focusing on chemical sensitization, electronic sensitization, and synergistic sensitization. Subsequently, the purification mechanism of contaminated gas is summarized, followed by a systematic overview of purifying polluted gases using SACs with a focus on photocatalysis and electrocatalysis. Last but not least, some issues in this research field are put forward and the corresponding solutions are suggested (Scheme 1).

2. Characterization of SACs

Structural identification of SACs heavily depends on characterization techniques.[32–35] Recent advancements in electron microscopy, structure-sensitive spectroscopy, and *in situ*/*operando* methodologies have led to a deep understanding of heterogeneous catalysis, including the structure of the catalyst and catalytic process.[36–41] Fig. 1 summarizes the commonly used techniques for characterizing structures of SACs at the atomic scale. The atomic structure of SACs can be probed by using high-resolution transmission electron microscopy (HRTEM) and scanning transmission electron microscopy (STEM). HRTEM enables direct visualization of individual atoms, revealing their sizes, shapes, and distributions. STEM, particularly when combined with energy dispersive X-ray spectroscopy (EDX), facilitates mapping of individual atomic elements on the supporting material to confirm their presence and provide information about their spatial distribution. The characterization of SACs' electronic structure primarily involves X-ray photoelectron spectroscopy (XPS), X-ray absorption spectroscopy (XAS), and infrared spectroscopy. XPS can offer insights into the oxidation states and electronic structure of individual atoms, facilitating comprehension of the interaction between single atoms and their support material as well as the impact on catalytic behavior. XAS, encompassing both X-ray absorption near edge structure (XANES) and extended X-ray absorption fine structure (EXAFS), can provide valuable information regarding the local structure and coordination environment of single atoms, thereby confirming their monatomic properties. Furthermore, infrared spectroscopy (IR), particularly when combined with CO as a probe molecule, can furnish details about adsorption sites on SACs while aiding in verifying the presence of single atoms and offering insights into their catalytic behaviors. These characterization methods, often used in combination, can provide comprehensive information about the structure, composition, and behavior of SACs. However, characterizing SACs is still challenging due to their unique nature, and ongoing research is aimed at developing more advanced characterization techniques for these materials.[42–44] A comprehensive understanding of the structure of SACs is crucial for designing more efficient SACs.[45–48] Fig. 2 illustrates the general process for determining whether a prepared catalyst is a SAC. Firstly, X-ray diffraction (XRD) analysis is performed to verify characteristic peaks corresponding to metal compounds in the sample. Subsequently, electron microscopy techniques including scanning electron microscopy (SEM), transmission electron microscopy (TEM), and high-angle annular dark-field scanning transmission electron microscopy (HAADF-STEM) are utilized to examine whether nanoparticles, sub-nanoparticles, or nanoclusters exist in the sample. Among these electron microscopy methods, HAADF-STEM provides high-quality imaging maps enabling identification of individual metal atoms through dispersed bright spots.[49–51] Finally, X-ray absorption spectroscopy (XAS) is employed to ascertain whether there exists metal–metal coordination. If all answers to these questions are "No", it indicates that the introduced metal atoms are atomically dispersed. A comprehensive analysis of the coordination structure of atomically dispersed metal atoms can be

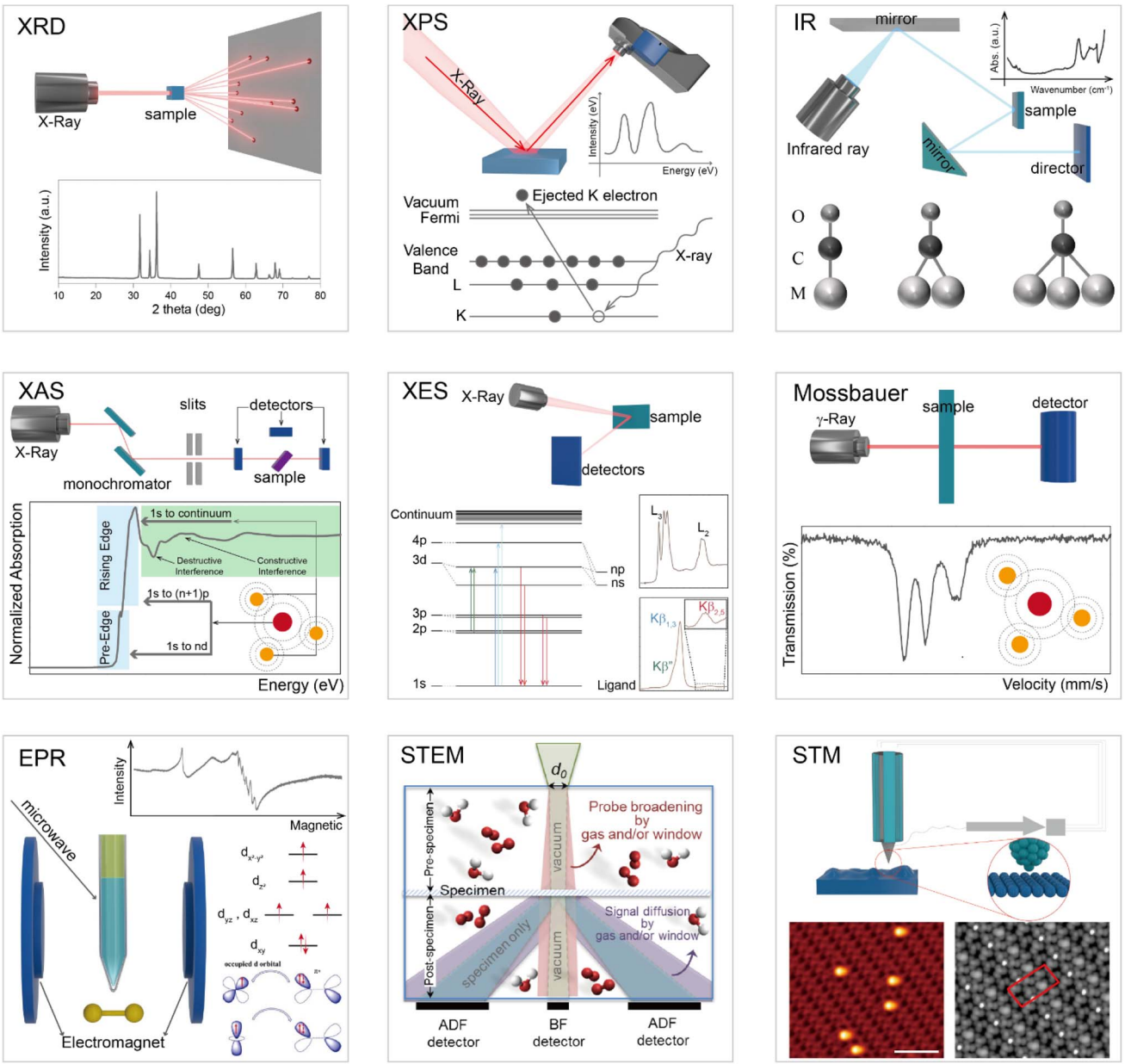

Fig. 1 Schematic illustration of different characterization methods for studying SACs.

conducted using various techniques, such as X-ray photoelectron spectroscopy (XPS) and X-ray absorption near edge structure (XANES) spectroscopy to determine the valence states of single atom centers in SACs; extended X-ray absorption fine structure (EXAFS) spectroscopy to get the coordination numbers; and X-ray emission spectroscopy (XES) together with density functional theory (DFT) calculation and spectroscopy simulation to obtain structural details.[52–56]

3. Application of surface acoustic wave (SAW) in gas detection

Since 1999, Kevin Ashton's development of the Internet of Things (IoT) has garnered significant recognition from technical communities and scientific experts. Sensors, serving as the fundamental building blocks of IoT, offer substantial advantages for studying diverse domains such as environmental conditions, climate patterns, human health status, food quality assessment, and water analysis. For instance, wearable sensors capable of detecting respiration or subcutaneous tissue can be employed for medical diagnostics; gas or water quality sensors can establish robust industrial safety measures and environmental monitoring systems; paper-based sensors enable instantaneous determination of food freshness and safety levels. However, despite their pivotal role in numerous scenarios, sensors still face challenges related to insufficient sensitivity, selectivity limitations, stability issues, and reliability concerns, which hinder their ability to meet expanding demands. Sensors still encounter difficulties in detecting trace

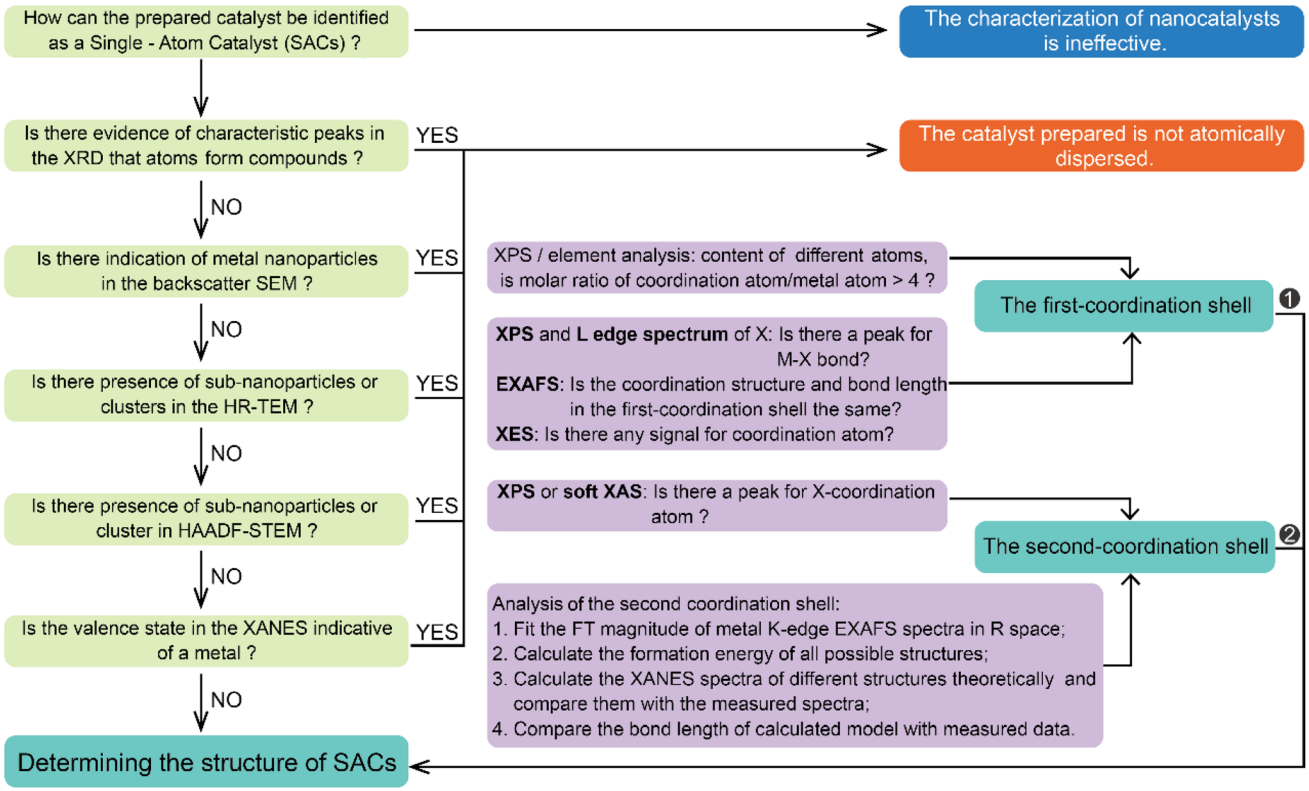

Fig. 2 The well-accepted protocol for determining the structure of SACs.

analytes at parts per billion (ppb) levels or lower concentrations while differentiating between similar compounds like methanol and ethanol. Therefore, it is imperative to develop highly sensitive sensors with strong selectivity that exhibit exceptional reliability and stability. One effective approach is to optimize the sensing material/catalyst. Precious metals such as Pt, Pd, and Ir, as well as metal oxides like ZnO, SnO_2, and Co_3O_4 are commonly employed as catalysts due to their unoccupied d-electron orbitals. However, the limited number of unsaturated coordination atoms on the surface of particle catalysts leads to low utilization of active sites. Reducing the size of metal nanoparticles is considered as an efficient strategy for increasing the number of catalytically exposed atoms, which consequently modifies the surface atomic structure, electron configuration, and surface defects. These alterations can generate favorable geometric and electronic effects on the coordination environment and enhance catalyst activity. A typical example illustrating this concept is single-atom catalysts (SACs), where active metal sites are isolated on a carrier or stabilized by a non-metallic ligand to maximize atomic utilization efficiency and catalytic activity. The significant enhancement of catalytic activity and selectivity in electrocatalysis, thermal catalysis, photocatalysis, and enzyme catalysis by SACs has been well established. These principles have paved the way for the development of various sensing methods such as electrochemistry, chemical resistance, colorimetry, luminescence, *etc.* In comparison to nanoparticles, nanoclusters, and bulk catalysts, SACs offer several advantages: (1) maximizing the utilization of catalytic metals while minimizing their consumption; (2) exhibiting unexpected stability and selectivity owing to their customizable coordination environment; (3) providing a comprehensive understanding of the mechanism behind the coordination environment. Although sensing with SACs is still at an early stage of development, remarkable progress has been made since 2016 with immense potential. Therefore, this section begins by providing a concise overview of the fundamental principles underlying gas sensors, followed by a comprehensive examination of three distinct mechanisms for enhancing gas sensitivity in single-atom catalysts, drawing upon recent advancements in the field of gas sensor research.

3.1 Working mechanism of gas sensors based on SACs

Gas sensors are typically made of metal oxides or conducting polymers, which exhibit changes in electrical conductivity when exposed to different gases.[57–59] The change in conductivity can be attributed to the change in electronic properties induced by adsorption/desorption of gas molecules on the surface of sensing materials.[60,61] Physisorption and chemisorption are two different types of adsorption processes that occur on the surface of semiconductors in gas sensors. They play a crucial role in the sensing mechanism of these devices. The process of physical adsorption involves the adherence of gas molecules to the sensor surface through weak van der Waals forces (or London dispersion forces). These relatively weak forces allow for reversible adsorption and desorption processes at low temperatures. Importantly, no chemical bonding forms between the

gas molecules and the sensor surface in physical adsorption. This non-specific process can occur for any gas molecules, and its capacity increases with increasing surface area. Additionally, physical adsorption typically results in multilayered adsorption as there is no limit to the number of layers that can be formed. The process of chemisorption involves the formation of a chemical bond between gas molecules and the sensor surface. This interaction is characterized by its increased strength and specificity compared to physical adsorption. During chemisorption, gas molecules undergo reactions with the sensor surface, resulting in the creation of new compounds. This process is typically irreversible and occurs at elevated temperatures. Chemisorption generally leads to monolayer adsorption as further adsorption becomes hindered once a monolayer is formed. In terms of gas sensors, both physisorption and chemisorption can influence their responses; chemisorption is often more desirable due to its ability to provide higher sensitivity and selectivity through specific interactions between gas molecules and the sensor surface. Several theories, such as the chemisorbed oxygen model,[62,63] grain boundary barrier model,[64,65] bulk resistance model,[66] space-charge layer model (electron depletion layer (EDL) and hole accumulation layer (HAL)),[67,68] can explain the variations in conductivity. These theories focus on electron transfer between gas molecules and semiconductor surfaces. When the electron affinity of the gas exceeds the work function of the semiconductor, electrons will be transferred from the semiconductor surface to adsorbed gas molecules, leading to the formation of adsorbed gas anions (Fig. 3a), which alters the electronic conductivity of the semiconductor.[69–71] In addition to the gas molecules adsorbed on the semiconductor surface, the chemisorbed oxygen species (O_2^-, O^-, O^{2-}) also play a crucial role in the gas sensor, significantly influencing the surface conductivity that is closely related to the operating temperature and type of semiconductor, and therefore these factors ultimately impact the characteristics of semiconductors in gas sensing applications.[60,62,72] The process of generating chemisorbed oxygen species on the semiconductor surface can be summarized by formulae (1)–(4).[73–76]

$$O_2(\text{gas}) \rightarrow O_2(\text{adsorbed}), (\text{air}) \quad (1)$$

$$O_2(\text{adsorbed}) + e^- \rightarrow 2O^-, (\text{air}, <150\ ^\circ\text{C}) \quad (2)$$

$$O_2(\text{adsorbed}) + e^- \rightarrow O_2^-, (\text{air}, 150\text{–}400\ ^\circ\text{C}) \quad (3)$$

$$O_2(\text{adsorbed}) + e^- \rightarrow O^{2-}, (\text{air}, >400\ ^\circ\text{C}) \quad (4)$$

For an n-type semiconductor, the gas–surface interaction can be explained as follows (Fig. 3b): initially, upon heating to a specific temperature, oxygen in the air is adsorbed onto designated sites on the semiconductor surface. Subsequently, the adsorbed oxygen molecules capture electrons from the semiconductor conduction band, forming chemisorbed oxygen species (O_2^-, O^-, O^{2-}) and simultaneously creating an EDL at the semiconductor–gas interface.[67,77–79] This EDL causes an increased electron transfer barrier. Reductive gases like ethanol can react with chemisorbed oxygen species to release electrons back into the semiconductor, thereby reducing the resistance.[80–82] After consumption of the chemisorbed oxygen species, oxygen molecules can be re-adsorbed onto the semiconductor surface to produce new oxygen anions until the reaction reaches

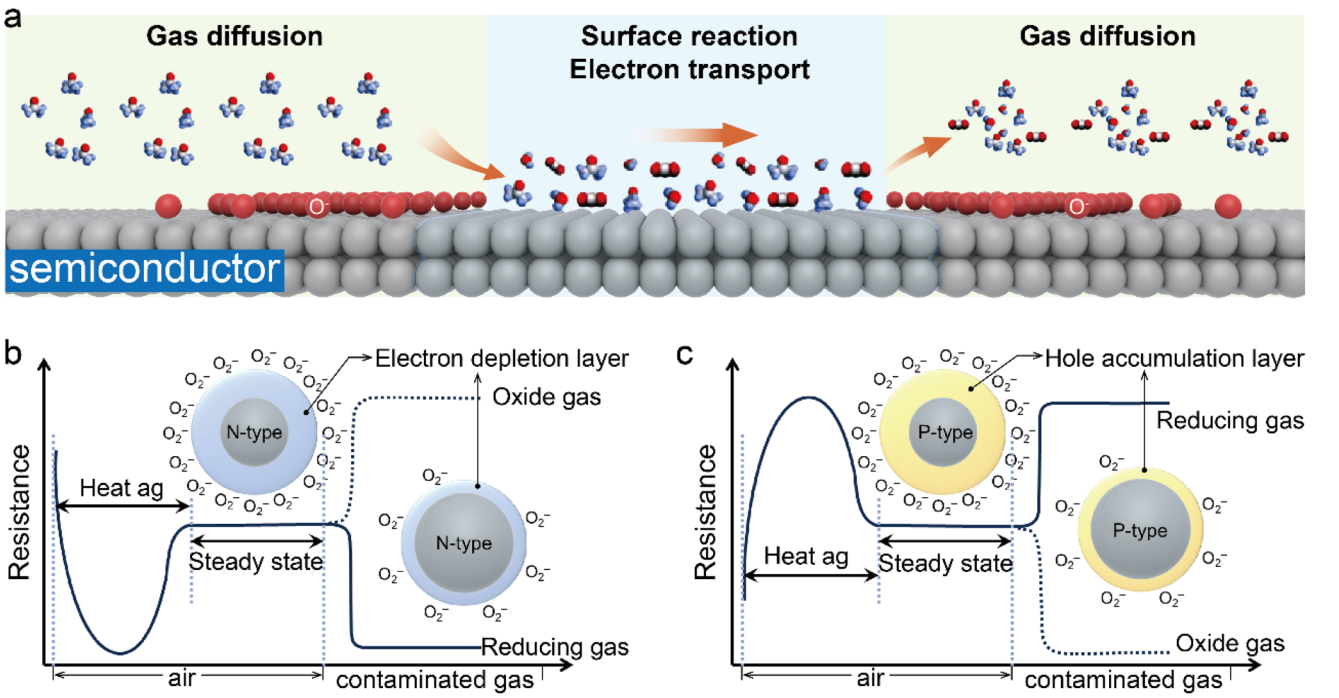

Fig. 3 (a) Schematic illustration showing the three steps taking place over a semiconductor for sensing gas molecules. Schematic diagram showing the detection principle of n-type (b) and p-type (c) semiconductors for sensing gas molecules.

equilibrium. Conversely, introducing an oxidizing gas will further deplete electrons and consequently increase the resistance in the semiconductor. For a p-type semiconductor, when it comes into contact with oxygen molecules (Fig. 3c), the oxygen molecules will capture electrons from the semiconductor valence band, converting them into chemisorbed oxygen ions.[83] Since the p-type semiconductor conducts current through holes, this loss of electrons leads to the formation of an HAL on the semiconductor surface and thus a reduction in the charge transfer barrier. When detecting reducing gases, these gas molecules react with adsorbed oxygen ions on the semiconductor surface, releasing electrons back into the semiconductor where they recombine with holes.[84] This reduces hole concentration and diminishes the hole accumulation layer, resulting in decreased conductivity and increased resistance in the semiconductor. Conversely, when oxidizing gases are detected, the oxidizing gas molecules can capture more electrons from the semiconductor, which will increase hole concentration and further enhance the conductivity while reducing the resistance. Gas detection is achieved by monitoring changes in resistance before and after gas exposure. The resistances of semiconductor gas sensors, whether n-type or p-type, are influenced by various factors. These factors can be categorized into internal and external factors. Internal factors primarily include the following aspects. (a) Doping level: the resistance of a semiconductor is directly correlated with its doping level. In n-type semiconductors, doping introduces additional free electrons, thereby enhancing the conductivity and reducing the resistance. Similarly, in p-type semiconductors, doping generates more holes which can also enhance the conductivity and reduce the resistance. (b) Temperature: the resistance of a semiconductor is temperature dependent. With increasing temperature, there is an increase in the number of free carriers (n-type electrons or p-type holes), resulting in a decrease in resistance. External factors mainly encompass: (a) gas concentration: when the semiconductor comes into contact with target gases within a gas sensor setup, its resistance changes accordingly. For an n-type semiconductor interacting with reducing (oxidizing) gases like CO (O_2), its resistance typically decreases (increases). For a p-type semiconductor, the resistance change is in the opposite direction to an n-type semiconductor. (b) Humidity: water vapor can affect the resistance of semiconductors by providing or accepting free carriers. (c) Crystal lattice structure: the surface morphology of semiconductors will impact the impurity concentration and grain boundary count; surfaces that are rougher with more grain boundaries tend to disperse carriers while increasing the impurity concentration.

In brief, the gas sensor system comprises of a sensor device, a conversion circuit, and a power supply.[85–88] The gas sensor device is responsible for detecting contaminated gases, while the conversion circuit transforms the chemical signal from the gas sensor into an electrical signal. The specific operation principle involves the adsorption or reaction of contaminated gas molecules onto a gas-sensitive material, leading to alterations in the resistance/current/voltage.[89–91] Thus, comprehending the sensitization mechanism of gas-sensitive materials is pivotal for investigating adsorption, chemical reaction, and desorption of oxygen molecules and polluted gases on semiconductor materials.[92–94] SACs serve as an exemplary platform for exploring these sensitization processes by offering novel insights into the sensitization mechanisms at the atomic level.[95] In the context of chemical sensitization, SACs exhibit unique catalytic properties in various chemical reactions due to their distinct electronic structure and unsaturated coordination environment. Additionally, SACs can provide active sites to adsorb oxygen and pollutant gas molecules, which may migrate to the surface of the sensing material through a phenomenon known as the surface spillover effect.[96,97] In terms of electronic sensitization, SACs form Schottky junctions with carriers by exploiting differences in band gap and work function, thereby facilitating electron transport.[98,99] Furthermore, SACs are able to react with oxygen to generate metal oxides and establish heterojunction interfaces with carrier materials. The manipulation of loss layers at these heterojunction interfaces can effectively regulate electron transport and ultimately enhance sensor performance.[100] For synergistic sensitization, SACs act as activation centers for oxygen molecules by modulating their activation kinetics.[101] Moreover, the activated oxygen molecules influenced by SACs can also impact gas sensitivity through an overflow effect.

3.2 Chemical sensitization of SACs

Chemical sensitization sensors for gas detection have been extensively investigated. Unlike electrochemical sensors, chemical sensitization sensor devices typically consist of a smaller number of interdigitated electrodes and metal oxide semiconductor (MOS) materials, eliminating the need for electrolyte and reference electrodes. Chemical sensitization sensors and electrochemical sensors are two commonly used gas detection systems, each with its own distinct advantages. In comparison to electrochemical sensors, chemical sensitization sensors possess the following advantages: (a) chemical sensitization sensors typically exhibit higher sensitivity and can be applied to detect extremely low concentration target gases. (b) Chemical sensitization allows for high selectivity towards specific gases by utilizing specific catalysts or active substances that only react with the target gases. This can reduce interference from other gases, a problem more frequently encountered in electrochemical sensors. (c) Chemical sensitization sensors offer superior long-term stability and are not affected by environmental conditions such as temperature and humidity, which can impact the performance of electrochemical sensors. (d) Chemical sensitization sensors usually operate without an external power support, making them more convenient and cost-effective for use in remote or hard-to-reach locations. (e) The design and manufacturing processes for chemical sensitization sensors are generally simpler. The resistance or direct current of chemical sensitization sensors is commonly measured by the galvanostatic or constant bias voltage method known as conductometry. To ensure accurate measurements, it is crucial for chemical sensitization sensors to exhibit appropriate conductivity. Insufficient conductivity will result in unmeasurable current or voltage drop. Pd single atoms (SAs) supported on TiO_2 exhibit a p-type characteristic that can generate active oxygen species (such as O_2^-)

from adsorbed oxygen, resulting in a state of high conductivity. TiO_2 is a widely used n-type semiconductor. By introducing Pt onto TiO_2, new energy levels can be created within the bandgap of TiO_2, which can generate hole carriers – a characteristic of p-type semiconductors. This occurs due to charge carrier modification and Schottky barrier formation between Pt and TiO_2, which separates electron–hole pairs and improves hole conductivity. Using p-type semiconductors in gas-sensitive applications offers advantages such as enhanced selectivity and sensitivity to certain types of gases. The catalytic activity of Pt can enhance the gas sensitive properties of the material by improving chemical reactions on its surface while also increasing oxygen vacancies that serve as electron capture sites thereby transforming TiO_2 into a p-type semiconductor. When reductive analyte CO molecules adhere to the Pd SAC, they undergo oxidation and release free electrons into the p-type Pd SAC, depleting hole carriers and leading to reduced conductivity. Upon removal of gaseous CO_2 molecules, oxygen molecules re-adhere and restore the high conductivity state of Pd SAC. Gas sensors based on conventional semiconductors such as ZnO, SnO_2, TiO_2, and In_2O_3 typically require high operating temperatures, resulting in increased energy consumption and limited applicability.[102–105] SACs offer advantages in chemical sensitization sensing due to their abundant active sites and exceptional oxygen adsorption ability,[106,107] which can enhance the catalytic spillover effect, leading to improved sensitivity and selectivity while reducing the required operating temperature.[108–110] For instance, in our previous study, Pt single atoms and Pt nanoparticles were deposited onto ZnO

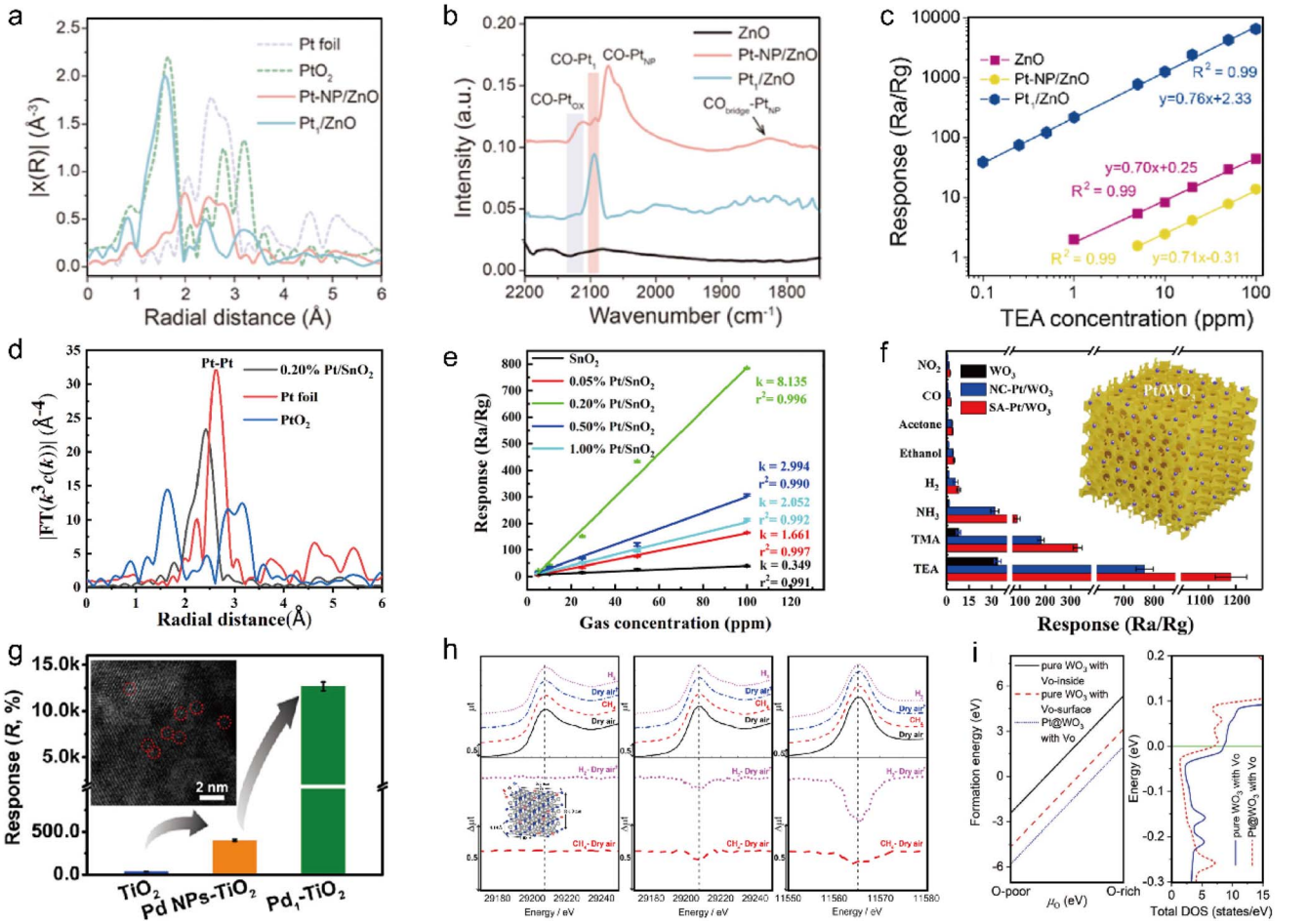

Fig. 4 (a) Fourier-transformed (FT) k^3-weighted EXAFS spectra of the Pt K-edge for Pt_1/ZnO, Pt-NP/ZnO, PtO_2, and Pt foil. (b) CO-DRIFTS of pure ZnO, Pt_1/ZnO, and Pt-NP/ZnO. (c) The linear relationship between response and TEA concentration within 0.1 to 100 ppm. Reproduced with permission from ref. 111 Copyright 2023, American Chemical Society. (d) EXAFS spectra in R space for Pt foil, PtO_2, and 0.2 wt% Pt/SnO_2. (e) Pt/SnO_2 sensor response to different TEA concentrations. Reproduced with permission from ref. 113 Copyright 2022, American Chemical Society. (f) Responses of the sensors to different gases (the concentrations of TEA, TMA and hydrogen are 50 ppm and the concentrations of other gases are 100 ppm. The operating temperature is 240 °C and the error bars represent the standard deviation (SD) of the responses for five independent determinations). Reproduced with permission from ref. 114 Copyright 2019, Elsevier. (g) Column charts of responses to 100 ppm CO over pristine TiO_2, Pd NPs–TiO_2, and Pd_1–TiO_2 nanoflowers. Inset shows an AC-HAADF-STEM image of Pd_1–TiO_2. Reproduced with permission from ref. 115 Copyright 2021, American Chemical Society. (h) XANES spectra of SnO_2 and 7.5 at% Pt–SnO_2 recorded at 703 K. Left: Sn K-edge of SnO_2, center: Sn K-edge, and right: Pt L_3-edge of Pt–SnO_2. Dry air in the figure means air treatment after CH_4 flow. Reproduced with permission from ref. 117 Copyright 2022, American Chemical Society. (i) Left: formation energies of V_O in pure WO_3 and Pt anchored WO_3 slab as a function of the chemical potential of O atom (μ_o). V_O-inside/surface indicates that the V_O is inside/at the surface of the WO_3 slab. Right: the total DOS of pure WO_3 and Pt anchored WO_3 slab with V_O. The Fermi level is set to zero. Reproduced with permission from ref. 120 Copyright 2022, Wiley-VCH.

using a dip-coating method as verified by EXAFS (Fig. 4a) and CO DRIFTS (Fig. 4b).[111] The Pt_1/ZnO gas sensor demonstrated a significant response to triethylamine (TEA) gas, while its responses to other gases were not prominent, indicating high selectivity of Pt_1/ZnO towards TEA. Conversely, both ZnO and Pt-NP/ZnO sensors showed low responses to all gases (Fig. 4c). The supports in SACs often possess porous structures with regular patterns that have high specific surface areas, facilitating efficient molecule/ion transport and enhancing the adsorption capacity to expand the resistance range.[112] Xiang *et al.* reported that the three-dimensional ordered mesoporous structure of SnO_2 (3DOM) was significantly enhanced by incorporating Pt.[113] EXAFS analysis revealed that atomically dispersed Pt predominated on the surface of 3DOM at a concentration of 0.20 wt% Pt/SnO_2 (Fig. 4d). This resulted in a large number of active sites, a high Hall mobility, and a great content of reactive oxygen species, while simultaneously reducing the response energy barrier. The sensor made of 0.20 wt% Pt/SnO_2 demonstrated exceptional performance with a low operating temperature of 80 °C and an impressive detection limit (0.32 ppb) for TEA (Fig. 4e). The gas sensing performance of Pt SAs could be significantly enhanced when loaded onto a three-dimensional ordered mesoporous WO_3, as demonstrated by Gu and co-workers (Fig. 4f).[114] Moreover, the limitations in sensitivity and selectivity commonly associated with chemical sensing materials at room temperature (RT) can be overcome by adjusting the surface coordination of SACs. The exceptional capability of Pd_1/TiO_2, which utilizes a solitary Pd atom to generate adsorbed O_2^-, along with its high efficiency and specificity for catalytic CO oxidation under ambient conditions, gives an unparalleled level of sensitivity compared to previously reported room temperature sensing materials.[115] This finding is reminiscent of observations made with other SACs employed for CO conversion (Fig. 4g). Generally, when SAs are loaded onto metal oxide semiconductor (MOS), their coordination with oxygen is fixed within the lattice structure.[116] This minimizes oxygen depletion during gas-sensitive reactions and allows for easy replenishment by atmospheric oxygen, leading to exceptional stability typically exhibited in SACs. Murata *et al.* demonstrated that Pt atoms dispersed randomly in a SnO_2 lattice underwent partial reduction without losing their lattice positions under reducing gases such as 1% CH_4 and 1% H_2.[117] *In situ* XAFS measurements showed no formation of Pt nanoparticles even during the reaction (Fig. 4h). For MOS, introducing SAs may cause loss of complete coordination between metal and oxygen atoms and result in incomplete metal–oxygen vacancy centers, however, these vacancies can be replenished from the surrounding air to maintain high stability.[118,119] The experimental phenomenon in the Pt_1/WO_3 system was confirmed by first-principles calculations, wherein the introduction of Pt SAs led to a reduction in Fermi level of WO_3 and an enhancement of its reactive oxygen capability (Fig. 4i).[120]

3.3 Electronic sensitization of SACs

Enhancement of gas response by tuning the concentration of charge carriers is referred to as "electronic sensitization". The formation of a Schottky junction between surface-active centers and carriers is crucial for enhancing electron transfer in electronic sensitization.[121,122] SACs possess unique properties to facilitate chemical reactions with high selectivity and efficiency. Additionally, SACs present in air can react with molecular oxygen to form metal oxides, creating heterojunctions with the carrier material.[123] Heterojunctions refer to interfaces between two different materials that have distinct electronic properties.[124–126] A heterojunction plays a significant role in modulating electron transport by altering the depletion layer between the two different materials. Precise control of the heterojunction can enhance sensor performance, opening possibilities for developing advanced sensing technologies capable of detecting various substances with high sensitivity and selectivity. According to a study conducted by Shin *et al.*, Pt SA-anchored carbon nitride nanosheets were integrated into a 1D nanofiber structure containing SnO_2 (Pt_1-N/CSnO_2).[127] The Pt_1-N/C site exhibited strong adsorption of O_2, with an adsorption energy of −1.93 eV. Furthermore, the O–O bond length of O_2 adsorbed on the Pt atom was longer compared to that on Pt bulk. These findings suggested easier adsorption and dissociation of O_2 on Pt SA in comparison to that on SnO_2, resulting in an increased concentration of chemisorbed oxygen species (Fig. 5a). The incorporation of Pt_1-N/C into SnO_2 led to a noticeable decrease of work function to 4.38 eV, indicating electron transfer from Pt_1-N/C to the main body of SnO_2. This observation supported the formation of the heterojunction as a second enhancement mechanism, where enhanced oxygen species adsorption occurred at the electron accumulation layer formed between SnO_2 and carbon nitride (Fig. 5b). Consequently, this increased the concentration of chemisorbed oxygen on the surface of Pt_1-N/C-SnO_2. Gas sensing tests showed that compared to the state-of-the-art formaldehyde gas sensors (Fig. 5c), Pt_1-N/C-SnO_2 gas sensor exhibited superior performance. Sun *et al.* developed a novel type of Pt_1/SnO_2@SiC multi-heterojunction, which demonstrated that the incorporation of Pt SAs into SnO_2 altered its electronic structure, resulting in efficient electron transfer within the formed heterojunction.[128] During gas sensing, the redox reaction between ethanol gas and ionized oxygen on Pt_1/SnO_2 generated electrons that were transferred to the heterojunction sensing material (Fig. 5d). The presence of Pt SAs significantly enhanced the electron transfer rate. Gas sensitivity tests revealed a significant improvement in ethanol detection performance for Pt_1/SnO_2@SiC (Fig. 5e). To elucidate the sensing mechanism, the carrier concentration of Fe_1/NC was measured by the Hall-effect measurement, and DFT calculations were performed based on an FeN_4 coordination structure (Fig. 5f).[129] DFT analysis showed that Fe_1/NC exhibited n-type semiconductor behavior with a band gap of 0.5 eV (Fig. 5g), consistent with the result obtained from the Hall effect measurement. Like n-type MOS gas sensing materials, it was anticipated that NO_2, as an oxidizing gas, would induce an increase in electrical resistance when interacting with Fe_1/NC. To clarify the selective response of the Fe_1/NC gas sensor towards NO_x, the adsorption structures and energies of various experimentally measured gases were further calculated by DFT (Fig. 5h). Based on the above research examples, it is evident that SACs hold immense potential in

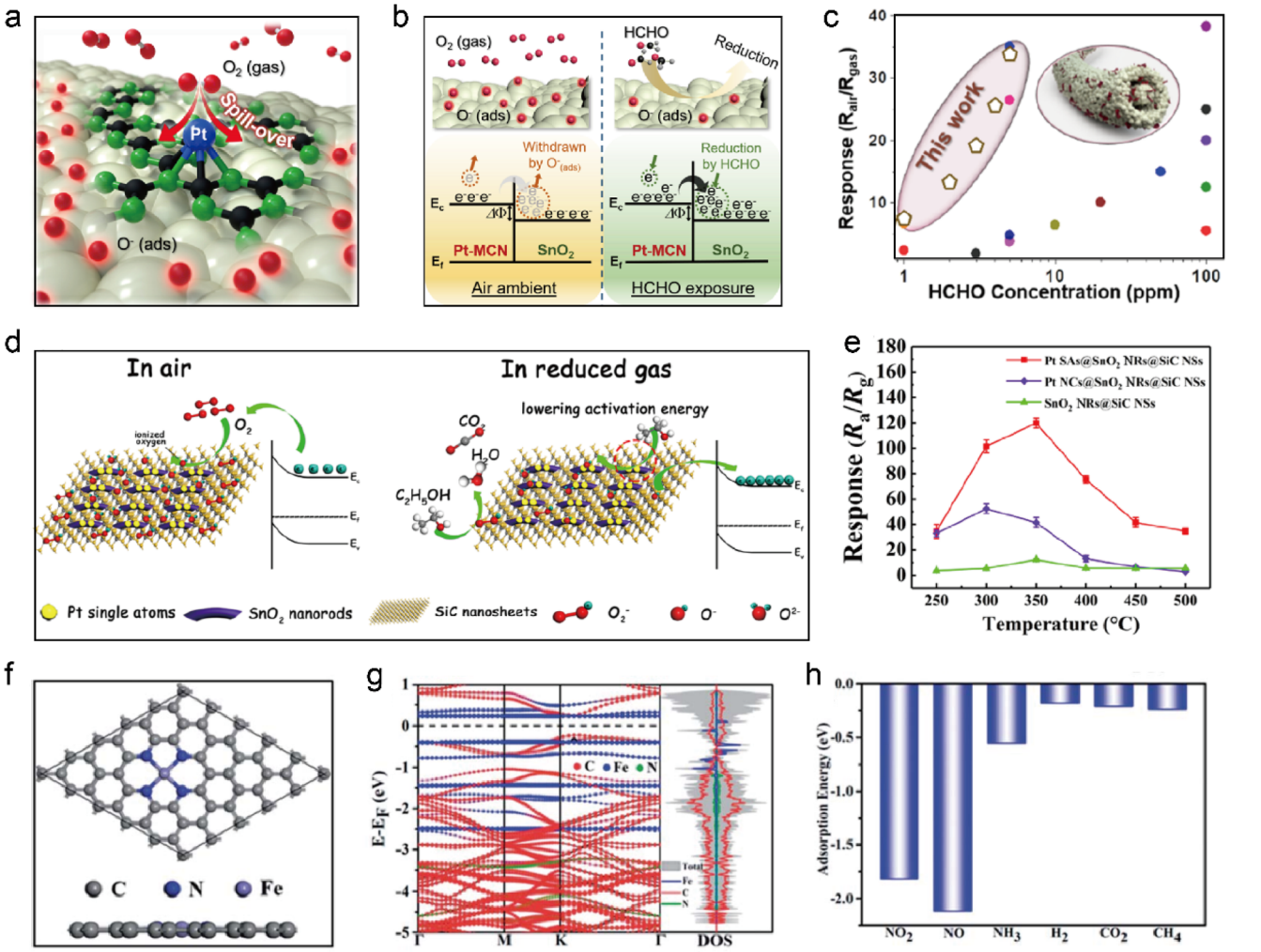

Fig. 5 (a) Schematic illustration of $O_{2(gas)}$ dissociation over Pt SAs on Pt–MCN–SnO_2 to form chemisorbed oxygen species ($O_{(ads)}^-$). (b) Schematic illustration showing the HCHO-sensing mechanism as well as the simplified energy band diagram of the heterojunction between MCN and SnO_2. (c) Comparison of the state-of-the-art formaldehyde gas sensors with that made of Pt–MCN–SnO_2. Reproduced with permission from ref. 127 Copyright 2020, American Chemical Society. (d) Schematic illustration showing the gas sensing mechanism of Pt SAs@SnO_2 NRs@SiC NSs. (e) Gas sensing response toward 500 ppm ethanol *versus* operating temperature over Pt SAs@SnO_2 NRs@SiC NSs, Pt NCs@SnO_2 NRs@SiC NSs, and SnO_2 NRs@SiC NSs. Reproduced with permission from ref. 128 Copyright 2020, American Chemical Society. (f) Top and side views showing the atomic configuration of FeNC in a 5 × 5 supercell. (g) Electronic band structure and density of states (DOS) for FeNC. (h) Adsorption energies of NO_2, NO, NH_3, H_2, CO_2 and CH_4 on FeNC. Reproduced with permission from ref. 129 Copyright 2020, Royal Society of Chemistry.

optimizing gas detection performance. Firstly, SACs possess unique electronic properties that enable efficient adsorption and transfer of electrical charges.[130] The distinctive electronic structure of SACs can not only enhance the catalytic activity, but also improve the selective recognition of gas molecules. Additionally, SACs also exhibit sensitivity to oxygen molecules, rendering them ideal candidates for gas detection.

3.4 Synergistic sensitization of SACs

The unique characteristics of SACs can facilitate effective interaction between gas molecules and single atomic active sites, thereby enhancing the probability of oxygen molecule adsorption and subsequent activation.[131] The increased sensitivity provided by SACs allows for faster and more precise detection of trace gases, particularly important when identifying harmful pollutants or volatile organic compounds (VOCs) at low concentrations. Moreover, an excess of reactive oxygen species may accumulate on the surface of SACs, resulting in rapid oxidation and removal of the target gas from the catalyst's surface. Xue *et al.* achieved highly sensitive NO_2 detection by dispersing Au atoms on a stepped ZnO surface (Au_1/ZnO) featuring abundant unsaturated terrace defects.[132] The electron transport associated with the sensing process was elucidated through theoretical studies. Fig. 6a illustrates the density of states (DOS) for ZnO, Au_1–ZnO, and Au_1/ZnO + NO_2. Upon introducing Au SAs onto ZnO, a new band gap becomes apparent, while the band gap of NO_2 widens significantly after adsorption on the ZnO surface, indicating an increase in

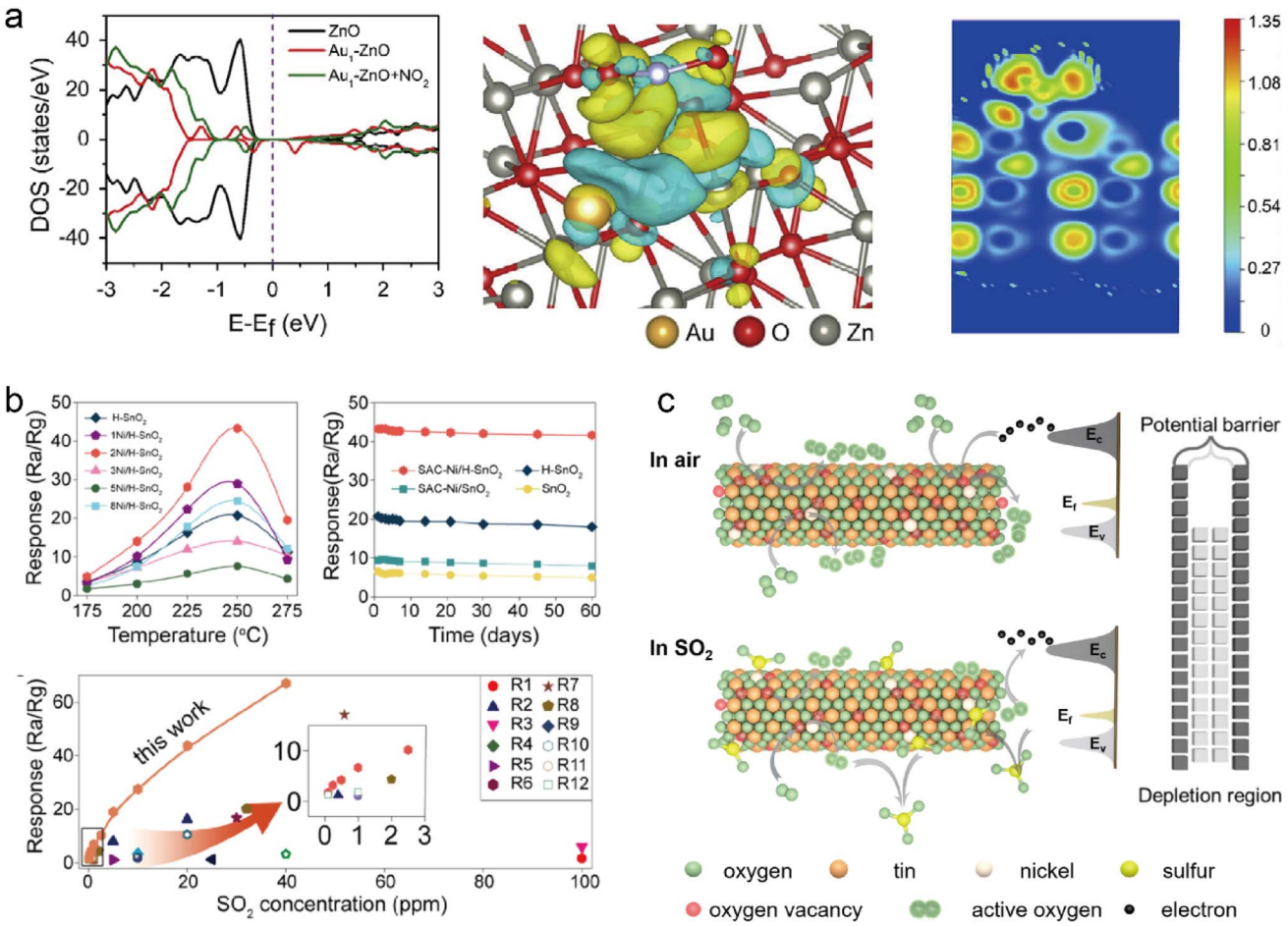

Fig. 6 (a) Left: calculated DOS for ZnO, Au_1–ZnO, and Au_1–ZnO + NO_2. Center: the charge density difference for Au_1–ZnO + NO_2. Right: schematic representation showing charge distribution in a two-dimensional plane. Reproduced with permission from ref. 132 Copyright 2020, Elsevier. (b) Top left: sensor's response to 20 ppm of SO_2 over 0–8 mol% Ni doped SnO_2 as a function of operating temperature at 40% RH. Top right: Long-term stability test at 250 °C. Bottom: comparison of state-of-the-art SO_2 gas sensors with that made of SAC-Ni/H-SnO_2. (c) Schematic illustration showing the gas sensing mechanism over SAC-Ni/H-SnO_2. Reproduced with permission from ref. 135 Copyright 2022, Elsevier.

resistance. The charge density analysis revealed that upon NO_2 adsorption on Au_1/ZnO, a substantial number of electrons were transferred from ZnO to NO_2, consistent with the DOS analysis results. Subsequent activation and oxidation occurred when O_2 was adsorbed on the Au SAs, leading to rapid detachment of NO_2 from the ZnO surface. This entire process caused a significant alteration in gas sensor resistance. This example clearly demonstrates that synergistic effects between O_2 adsorption at the Au SA site and NO_2 adsorption on ZnO surface can enhance gas sensing performance. Furthermore, SACs based on MOS, which exhibit selective adsorption of certain gas molecules over single metal atom active sites, in contrast to vacancies on the MOS support that often generate ROS to excite and catalyze reactions, may achieve high sensing performance.[133,134] For example, we demonstrated an ultra-sensitive gas sensor to detect SO_2 that used atomically dispersed Ni on oxygen vacancy rich SnO_2 nanorods (SAC-Ni/H-SnO_2) as the sensing material.[135] As shown in Fig. 6b, all tested sensors show the highest response to SO_2 at 250 °C, among which, SAC-Ni/H-SnO_2 (2 mol% Ni loaded H-SnO_2) displays the highest gas sensitivity. Fig. 6c presents the 60 days stability test of the gas sensor. After 60 days, the SO_2 response of the gas sensor made of SAC-Ni/H-SnO_2, H-SnO_2, SAC-Ni/SnO_2 and SnO_2 decreased by 4.6%, 13.4%, 15.9% and 24.5%, respectively, reflecting long-term stability of the SAC-Ni/H-SnO_2 gas sensor. Based on *in situ* electron paramagnetic resonance (EPR) and *in situ* infrared (IR) spectroscopy measurements, it was revealed that the adsorbed SO_2 could effectively react with the abundant superoxide free radicals on the SAC-Ni/H-SnO_2 surface, resulting in a reduction of the electrical double layer thickness and sensor resistance through efficient release of trapped electrons. Hence, it can be concluded that the synergistic effect between Ni-SAC and oxygen vacancy makes SAC-Ni/H-SnO_2 exhibit high sensitivity and selectivity to SO_2 (Fig. 6b).

To summarize, the use of SACs can significantly enhance gas sensing performance *via* chemical sensitization, electronic sensitization and synergistic sensitization mechanisms, enabling gas sensors to operate at room temperature and

Table 1 Advantages and disadvantages of SACs for the gas sensing performance

Advantages	Disadvantages
High efficiency	Preparation complexity
Exceptional selectivity	Poor durability
Superior stability	Low sensitivity
Cost-effective	High cost of precious metal-based SACs
Environmentally friendly	Limited understanding of the SAC mechanisms

thereby enhancing their safety, energy efficiency, and environmental friendliness.

3.5 Advantages/disadvantages of SACs for gas sensing

SACs represent a novel frontier in heterogeneous catalysis, owing to their distinctive properties and potential applications across various fields, including gas sensing. As shown in Table 1, we highlight the advantages and disadvantages of using single atom catalysts for gas sensing performance. SACs demonstrate high catalytic efficiency as each atom functions as an active site, thereby significantly enhancing the gas sensing performance. Moreover, the unique electronic and geometric structures of SACs enable exceptional selectivity towards specific gases. Additionally, SACs exhibit superior stability compared to conventional catalysts, resulting in prolonged sensor lifetimes. Furthermore, despite the potentially higher initial cost, the long-term cost-effectiveness of SACs is enhanced due to their excellent efficiency and stability. However, the preparation of SACs is complex which requires precise control over the synthesis conditions. While SACs are generally stable, they can exhibit susceptibility to aggregation under specific conditions, resulting in reduced catalytic activity and compromised gas sensing performance. The sensitivity of SACs can be influenced by various factors, such as the type of support material. The high cost associated with SACs, particularly those based on precious metals, poses a disadvantage for their widespread utilization in gas sensing applications. Additionally, limited understanding of the mechanisms underlying SACs hinders their optimization and application in the field of gas sensing.

4. Catalytic properties of SACs

With the rapid advancement of industrialization, urbanization, and global population growth, along with extensive utilization of fossil fuels and the impact of climate change, the issue of contaminated gas has become increasingly severe. Consequently, there is a growing emphasis on research aimed at discovering efficient, cost-effective and environmentally friendly technologies for mitigating contaminated gas emissions to our surrounding environment. Among the gas purification technologies that have been developed, advanced

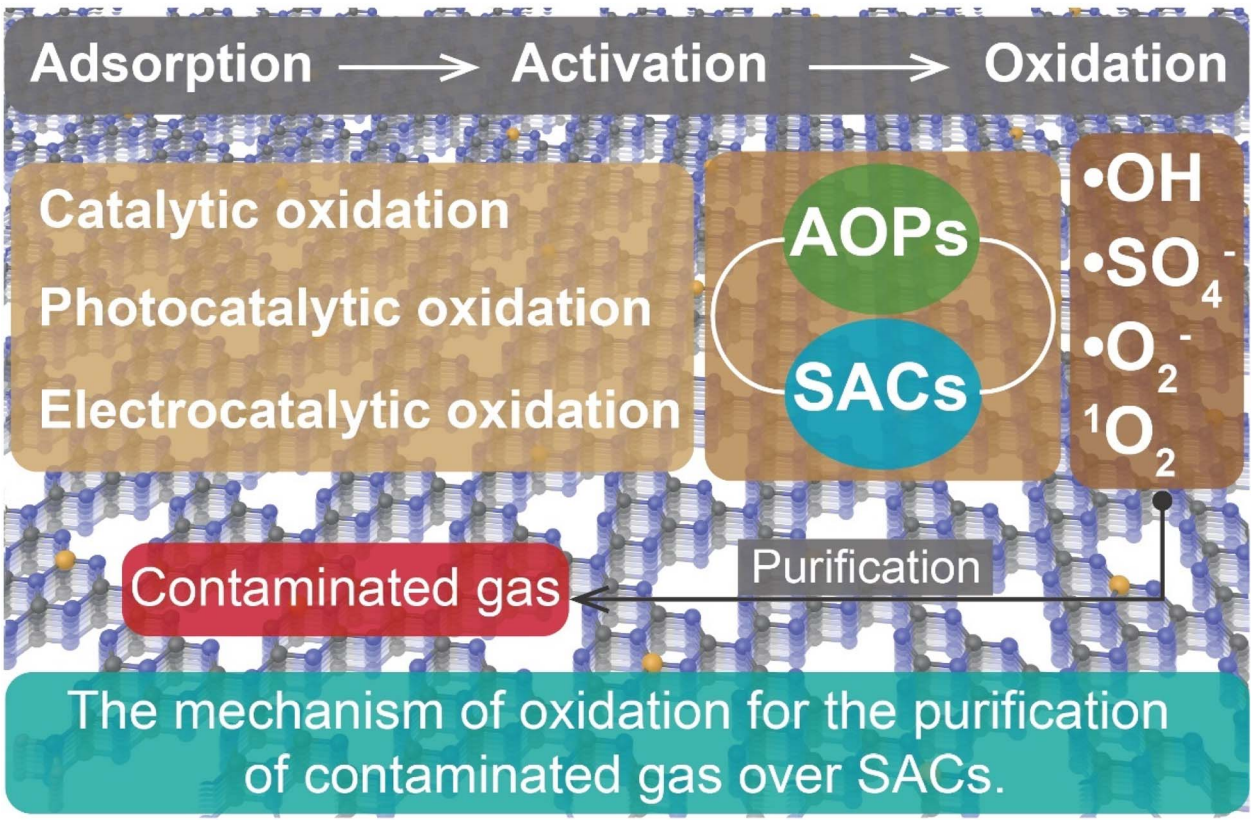

Fig. 7 The catalytic mechanisms of SACs in various AOPs.

oxidation processes (AOPs) show excellent performance.[27,136,137] AOPs possess the ability to break down persistent contaminants through the generation of highly reactive oxygen species (ROS), including hydroxyl radical ($^{\bullet}OH$), sulfate radical ($^{\bullet}SO_4^-$), superoxide radical ($^{\bullet}O_2^-$), *etc.*[138–140] Based on the external energy supply methods, the AOP system can be categorized into catalytic oxidation, photocatalytic oxidation, and electrocatalytic oxidation. In the following section, we will focus on the recent advancements in utilizing SACs for gas purification, elucidating the catalytic mechanisms of SACs in various AOPs, and examining the prospective opportunities and research directions for further developing SACs in the field of gas purification (Fig. 7).

4.1 Catalytic oxidation reactions of contaminated gas over SACs

The oxidation reactions can effectively convert contaminated gases into non-toxic substances that are in alignment with stable elements, leading to fewer secondary pollutants compared to other treatment methods (Fig. 8a).[141] However, the oxidation treatment typically requires a high reaction temperature and consumes a significant amount of energy (Fig. 8b).[142,143] This dependence not only escalates the energy demand but also presents challenges in terms of equipment design and operation. To surmount these limitations, researchers have been exploring alternative approaches to mitigate the requirement for high reaction temperature while maintaining efficient catalytic oxidation. Another extensively studied strategy entails advancing catalytic reactions such as novel photocatalyses and electrocatalyses, which rely on natural sunlight or renewable electricity, rendering them clean and sustainable recycling technologies.

Recently, significant advancements have been made in the development of high-performance SACs for AOPs.[144–146] These SACs demonstrate superior performance compared to nanoparticle counterparts.[147–150] For instance, Ag SAs loaded on hollandite manganese oxide (Ag_1/HMO) achieved complete benzene oxidation at 220 °C at a gas space velocity (GHSV) as high as 23 000 h^{-1} (Fig. 8c).[151] The isolated Ag atoms exhibited exceptional ability in activating lattice oxygen and gaseous O_2 due to their upshifted 4d orbitals. Incorporation of Ag atoms onto cryptomelane-type manganese oxide (K/Ag-OMS-40) resulted in an even higher rate of benzene conversion along with excellent stability and enhanced resistance against chlorine poisoning and moisture compared to the catalyst of 1 wt% Pd supported on Al_2O_3.[152] This enhancement could be attributed to an increased number of Mn octahedral defects and newly formed Ag–O–Mn interaction entities that expedited charge transfer and facilitated efficient benzene conversion. The atomically dispersed noble metal atoms can also promote HCHO oxidation at low temperature. For example, introducing Au SAs onto α-MnO_2 and CeO_2 to form Au_1/α-MnO_2 and Au_1/CeO_2 catalysts significantly enhanced their activity and stability by facilitating the formation of oxygen vacancies, generating active oxygen species, and providing charged Au species as active sites.[153,154] At 75 °C, Au_1/α-MnO_2 catalyst could completely decompose 500 ppm HCHO stream with a WHSV of 60 L g^{-1} h^{-1}. On the other hand, among the various CeO_2 morphologies tested, Au SAs on CeO_2 nanorods exhibited optimal catalytic

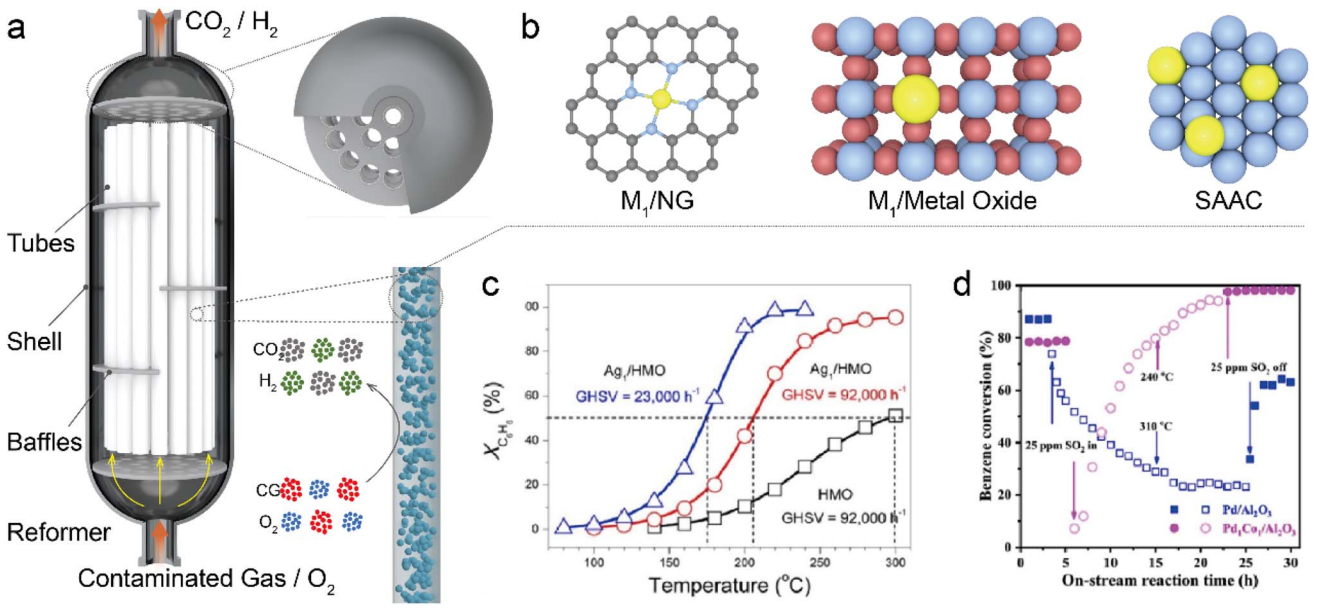

Fig. 8 (a) A schematic diagram illustrating a catalytic oxidation reactor designed for purification of contaminated gas. (b) A diagram showing different types of single-atom catalysts. (c) Conversion of benzene ($X_{C_6H_6}$) as a function of temperature over Ag_1/HMO at different gas hourly space velocities (GHSVs) and $X_{C_6H_6}$ of HMO at a GHSV of 92 000 h^{-1} is also given for comparison. Reaction conditions: benzene, 200 ppm; O_2, 20% balanced by N_2; flow rate, 100 mL min^{-1}. Reproduced with permission from ref. 151 Copyright 2017, American Chemical Society. (d) Benzene conversion as a function of on-stream reaction time in the presence or absence of SO_2 over the as-obtained samples. Reproduced with permission from ref. 158 Copyright 2021, Elsevier.

performance with achieving complete mineralization of HCHO at 85 °C. Besides Au SACs, Pt_1/MnO_2 catalyst could achieve full conversion of indoor-level toluene at ambient temperature thanks to the generation of surface-active oxygen species (*e.g.*, ·OH).[155] Chen *et al.* identified 0.47 wt% $Pt_1/Mn–TiO_2$ as an exceptional catalyst with remarkable activity for complete elimination of HCHO (100 ppm) at room temperature under the conditions of WHSV = 60 L $(g\ h)^{-1}$ and RH = 50%.[156] Furthermore, non-noble metal SACs have also been studied for contaminated gas decomposition. Through DFT calculations, Liu *et al.* proposed that Al SAs on graphene could be a potential catalyst for room temperature oxidation of HCHO *via* a pathway involving the formation of HCOOH followed by CO and subsequent CO_2 release.[157] The energy barriers associated with breaking C–H bonds in HCHO and C–O bonds in HCOOH were both determined to be 0.82 eV, which served as the kinetic limiting steps during the reaction process. To deeply understand the mechanism of SACs in AOPs, *in situ* experiments such as *in situ* diffuse reflectance infrared Fourier transform spectroscopy (DRIFTS) and *in situ* X-ray absorption spectroscopy (XAS) are unusually performed. For example, Hou *et al.* prepared a bimetal single-atom Pd_1Co_1/Al_2O_3 catalyst, in which the Co_1 sites rapidly generated O═Co═O species for oxygen activation, while the Pd_1 sites exhibited selective adsorption of benzene with excellent sulfur resistance.[158] The Pd_1Co_1/Al_2O_3 catalyst thus showed favorable catalytic performance for benzene oxidation with approximately 90% conversion at 256 °C, and demonstrated gradual recovery after exposure to 25 ppm SO_2 gas (Fig. 8d). Previous research has demonstrated that due to the π-bond in benzene, it adopts a parallel or planar configuration on densely packed transition metal surfaces. The presence of both Pd_1 and Co_1 active sites effectively hindered competitive adsorption between benzene and oxygen, thereby enhancing the reactivity. Additionally, in another study, upon introduction of SO_2, the PdO–SO_3 complex decomposed into PdO, reactive oxygen species (ROS), and aluminum sulfite at low temperatures.[159] ROS and PdO sites continued to participate in the reaction, resulting in exceptional sulfur resistance.

4.2 Photocatalytic oxidation reactions of contaminated gas over SACs

SACs can also greatly promote photocatalytic oxidation performance.[160] A typical photocatalytic system consists of two essential components: a catalytically active site and a light-harvesting unit.[161] In the case of SA photocatalysts, metal SAs act as the catalytically active sites, while the support serves as the light-harvesting unit. Therefore, the interaction between metal SAs and the support in these single-atom photocatalytic systems plays a crucial role in determining charge-transfer dynamics during photocatalytic reactions, which ultimately governs the overall photocatalytic performance.[162] It is also important to note that the SAs in photocatalysis may have roles beyond being solely catalytically active sites. For specific photocatalytic reactions, atomically dispersed SAs in SACs can be utilized to enhance the activity and selectivity while simultaneously improving the capacity for absorbing light and facilitating charge transfer. SACs can influence three crucial steps in a photocatalytic reaction, namely light harvesting, charge separation/transfer, and surface catalysis (Fig. 9a–c). Particularly, the presence of SAs on a semiconductor material can modify its electronic structure, thereby changing the light absorption properties of the semiconductor. For example, coordinating Co^{2+} atoms with g-C_3N_4 could extend light absorption up to 800 nm (Fig. 9d).[163] The phenomenon of enhanced light absorption has been widely observed in various single-atom photocatalyst systems. For instance, Ye and colleagues demonstrated a noticeable red-shift in the light absorption spectrum of CdS by decorating CdS nanowires with Pt SAs *via* the Pt–S bond.[164] A similar effect was also observed in MOS. Lee *et al.* showed that incorporating Cu SAs onto TiO_2 hollow spheres led to significantly improved light absorption across all measured wavelengths (300–800 nm).[165] They attributed this enhancement to the valence state change of Cu SAs, which effectively modulated the local TiO_2 lattice. Despite these findings, the exact mechanism responsible for the enhanced light absorption induced by metal SAs remains a subject of debate. As a result, further investigation into the role played by metal SAs is highly warranted. The efficacy of the entire photocatalytic process heavily depends on the charge transfer dynamics between single metal atoms and their semiconductor support. The successful separation and transfer of photogenerated electrons and holes at the metal–semiconductor interface are pivotal for achieving optimal photocatalytic performance.[166] When a metal contacts a semiconductor, an electronic equilibrium is established, enabling photogenerated electrons in the semiconductor to transfer *via* the formed Schottky junction to the supported metal SAs. This distinctive process of charge carrier separation across the metal–semiconductor interface can be fully harnessed by single-atom photocatalysts. Interestingly, reducing the size of metal nanoparticles to individual metal atoms can significantly impact their electronic structures and modify their interactions with support materials, ultimately influencing the charge transfer between light-harvesting materials and the individual atoms. For example, our research discovered that seamless integration of g-C_3N_4 with solitary Co^{2+} ions allowed for coordination of the light absorption unit with the catalytic site.[163] Photogenerated holes were predominantly located at the atomically dispersed Co sites, while photogenerated electrons were primarily located at the g-C_3N_4 framework. As a result, when carriers migrated from g-C_3N_4 to atomically dispersed Co sites, it greatly suppressed carrier recombination. This led to a substantial enhancement in photocatalytic performance (Fig. 9e). Surface reactions play a crucial role in determining the photocatalytic activity and selectivity. Typically, these reactions are influenced by the geometric and electronic structure of the photocatalytic system. The adjustable surface structure of different supports provides diverse coordination environments for SAs. Consequently, it is possible to manipulate the geometric and electronic properties of single-atom photocatalysts through interactions with the support material, thereby allowing modification of the adsorption configurations of reactants, intermediates, and products as well as altering the reaction

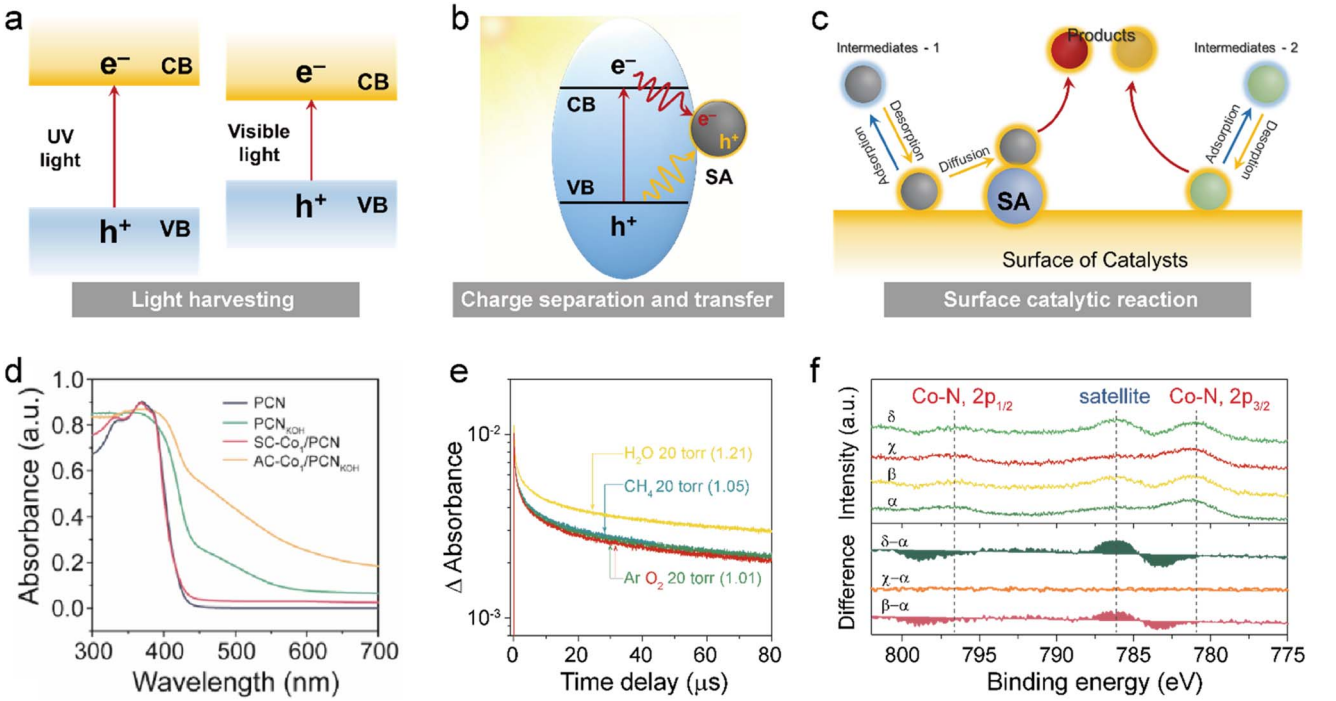

Fig. 9 The role of SACs in influencing three key steps of a photocatalytic reaction, namely (a) light harvesting, (b) charge separation and transfer, and (c) surface catalytic reaction. (d) UV-vis diffuse reflection spectra of CN, PCN, Co_1/CN, and Co_1/PCN. (e) The comparison of *in situ* transient absorption decay on AC-Co_1/PCN_{KOH} at 10 000 cm^{-1} under Ar, CH_4, O_2, and H_2O atmospheres (20 torr). (f) Co 2p NAP-XPS spectra of AC-Co_1/PCN_{KOH} when introducing 1 mbar of Ar (α), Ar + H_2O (β), CH_4 (χ), and CH_4 + H_2O (δ) at room temperature. Reproduced with permission from ref. 163 Copyright 2023, Elsevier.

pathway.[167] Compared to nanoclusters, nanoparticles, and bulk materials, SAs possess unique coordinatively unsaturated sites with distinctive electronic structures that can offer abundant active surface sites for catalyzing chemical reactions. Our research revealed that carbon nitride-supported cobalt SAs (C-C_2N_2) with asymmetric coordination exhibited a desired electronic configuration for single-electron transfer water oxidation reaction during photocatalysis, as demonstrated by near ambient-pressure XPS (NAP-XPS) measurements (Fig. 9f), *in situ* XPS analysis, and time-dependent DFT calculations.[163] Consequently, this unique Co-C_2N_2 photocatalyst significantly enhanced the selectivity of CH_4 oxidation to CH_3OH under visible light illumination.

Single-atom photocatalysts have demonstrated encouraging performance in oxidizing contaminated gas under light illumination.[168–170] Furthermore, coupling photocatalysis with other molecules (*e.g.*, H_2O_2 and PMS) to form more oxidative radicals with stronger oxidation capability is conducive to enhancing the photodegradation performance.[171,172] Additionally, photo-thermocatalysis offers another powerful technique for environmental remedy.[173–175]

4.2.1. Photocatalysis alone. Atomically dispersed metal sites on various semiconductors have been shown promising to promote the photocatalytic performance through tuning the band structure, and charge separation/transfer properties. Graphitic carbon nitride (GCN) is a commonly used substrate to support SAs to construct single-atom photocatalysts.[176] Our research found that an antimony single-atom photocatalyst (Sb-SAPC, single Sb atoms dispersed on carbon nitride) could effectively produce H_2O_2 in water and ambient air under visible light irradiation, which could be used to oxidize gaseous pollutants.[177] Zhang *et al.* dispersed single Zn atoms into the interlayer of g-C_3N_4 (Zn-CN-0.5) through a simple pyrolysis method.[178] XAFS and DFT studies revealed that Zn-CN-0.5 possessed a coordination structure of Zn–N_3 (Fig. 10a), which could enhance visible light absorption and electron–hole pair separation. As a result, Zn-CN-0.5 displayed greatly enhanced photocatalytic activity to purify NO as compared to pure GCN and Zn cluster-GCN (Fig. 10b). Besides GCN, oxides can also be used as supports to fabricate single-atom photocatalysts. Wu *et al.* anchored Pt single atoms onto TiO_2 nanosheet-assembled hierarchical spheres (Pt_1/TiO_2-HS).[179] The as-prepared Pt_1/TiO_2-HS showed excellent and stable photooxidation activity of HCHO (Fig. 10c). Chen *et al.* developed atomically dispersed Er on TiO_2 photocatalyst (Er_1–TiO_2).[180] Thanks to the outstanding separation of electron–hole pairs, Er_1–TiO_2 could degrade *o*-xylene and acetaldehyde with a conversion ratio of 90% and 100%, respectively under light illumination (Fig. 10d). Mori *et al.* prepared single-atom Eu^{3+} doped g-C_3N_4 nanosheets (Eu/g-C_3N_4).[181] The Eu^{3+} ion doping not only altered the optical properties of g-C_3N_4, but also exhibited characteristic single-atom Eu^{3+} emissions due to the $^5D_0 \rightarrow {}^7F_J$ transitions (J = 0–4). As a result, Eu/g-C_3N_4 showed a 12-fold activity increase in cyclohexane removal as compared to pure g-C_3N_4. Xia *et al.*

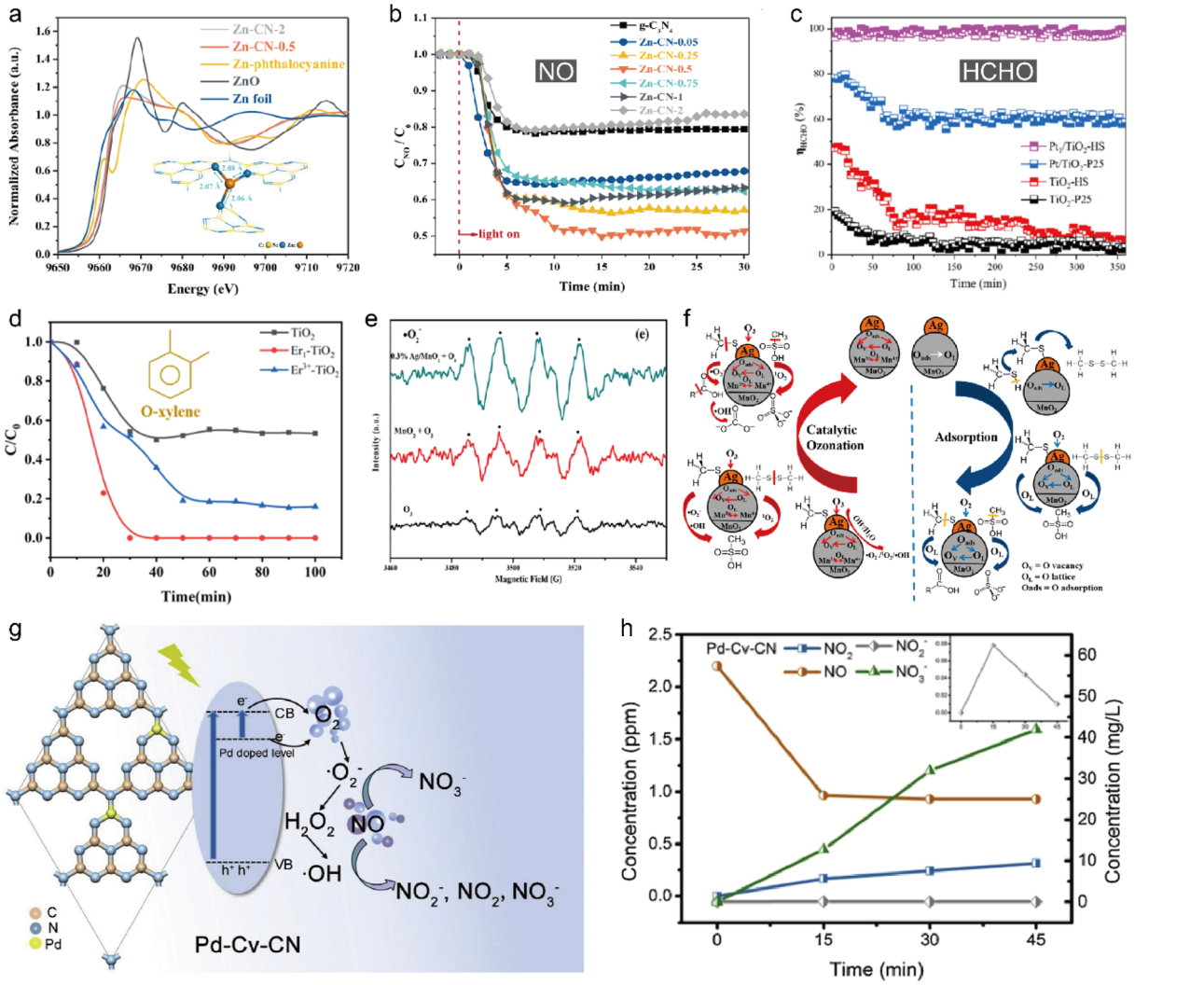

Fig. 10 (a) XANES spectra of different Zn–CN samples. Inset shows the DFT-calculated Zn–CN structure. (b) NO oxidation over different Zn–CN samples. Reproduced with permission from ref. 178 Copyright 2023, Elsevier. (c) HCHO removal efficiency. Reproduced with permission from ref. 179 Copyright 2023, Elsevier. (d) The dynamic degradation curves for *o*-xylene. The initial concentration of *o*-xylene was 50 ppm. The flow rate of *o*-xylene and air was 20 sccm. 0.1 g photocatalysts was used. Reproduced with permission from ref. 180 Copyright 2022, Elsevier. (e) EPR signal of superoxide radical. (f) Adsorption and catalytic ozonation pathway of CH_3SH over Ag/MnO_2 PHMSs. Reproduced with permission from ref. 182 Copyright 2018, American Chemical Society. (g) Light-induced charge separation and the proposed mechanism for photocatalytic oxidation of NO over Pd-Cv-CN. (h) The evolution of NO and its oxidation products (NO_2^-, NO_2, NO_3^-) with irradiation time over Pd-Cv-CN. All of the experiments were conducted under the same conditions: 2.2 ppm NO at a flow rate of 1.7 L min^{-1} was irradiated by a 300 W Xe lamp at 298 K with a relative humidity *ca.* 50%. Reproduced with permission from ref. 184 Copyright 2021, Elsevier.

reported single-atom Ag incorporated porous hollow microspheres (Ag/MnO_2 PHMSs) for CH_3SH removal in air.[182] The Ag/MnO_2 PHMSs could completely degrade 70 ppm CH_3SH within 600 s under light illumination. Electron spin resonance (ESR) and scavenger experiments indicated that ·OH and $^1O_2$ were the main reactive oxygen species engaging in methyl mercaptan degradation (Fig. 10e). The experimental results show that methyl mercaptan was decomposed into decarboxylation and sulfate ion, which finally turned into the harmless SO_4^{2-}, CO_2 and H_2O (Fig. 10f). Besides noble metals, transition metals have also been used to fabricate single-atom photocatalysts. Hu *et al.* grew single Fe atoms onto TiO_2 hollow microspheres to construct Fe_1/TiO_2-HMSs for the removal of NO.[183] The Fe–O bonds and Fe–Ti bonds formed in Fe_1/TiO_2-HMSs ensured robust interaction between single Fe atoms and TiO_2. Owing to the enhanced light adsorption, increased electron density and facilitated charge separation, Fe_1/TiO_2-HMSs demonstrated excellent NO removal rate under visible light irradiation with a NO removal rate as high as 47.91%, 2.3 times that of pure TiO_2. Liu *et al.* fabricated g-C_3N_4 with a controlled number of carbon defects to manipulate the distribution of single-atom Pd by leveraging its affinity to nitrogen atoms resulting from carbon vacancies.[184] The obtained photocatalyst exhibited exceptional and durable photocatalytic activity in NO conversion, surpassing pristine g-C_3N_4 by approximately 4.4 times. The improved photoactivity was attributed to the preferential

separation and transport of photogenerated charge carriers due to the introduction of Pd SAs (Fig. 10g and h).

4.2.2. Photo-Fenton reactions. Photo-Fenton reaction emerges as a promising strategy to remove pollutants due to the strong oxidation power of ·OH.[185,186] Wang *et al.* synthesized pyrrolic-type FeN_4 supported on g-C_3N_4 for VOC removal.[187] The pyrrolic-type FeN_4 displayed better photo-Fenton activity than pure g-C_3N_4 and pyridinic-type FeN_4 in a wide window of pH. Bader charge and differential charge distribution analyses disclosed that charge distribution was more favored over pyrrolic-type FeN_4 (Fig. 11a). DFT calculations further confirmed that pyrrolic-type FeN_4 was more stable and had higher intrinsic activity for the photo-Fenton reaction than pyridinic-type FeN_4. Wu *et al.* chelated Fe(III) single atoms onto amidoxime with an Fe loading of 24.04 wt% (U-g-PAO/Fe), which exhibited excellent removal of H_2S within 35 min *via* activating H_2O_2 under visible light.[188] Furthermore, the outstanding activity could maintain over a wide pH range from 2 to 10, superior to typical Fenton catalysts. XAFS and DFT calculations disclosed that [amidoxime-Fe(OH)$(H_2O)_3]^{2+}$ was the active site to activate H_2O_2 to produce ·OH (Fig. 11b). H_2O_2 activation was directly associated with the metal center, and thus tuning the charge state of the metal center in SACs offers a powerful strategy to improve their catalytic activity.[189] Zhan *et al.* introduced N vacancies into a single-Fe-atom photocatalyst (Fe_1-N_v/CN) to boost the activation of H_2O_2 (Fig. 11c).[190] According to transient absorption spectroscopy measurements and DFT calculations, the N vacancies acted as the electron trap, propelling electrons to accumulate on single Fe atoms. The high electron density over the single Fe atomic sites was able to enhance H_2O_2 activation. As a result, the catalyst exhibited an 18-fold activity increase in degrading ciprofloxacin gas as compared to pure CN. Besides Fe, other elements were also exploited for photo-Fenton reactions. A series of M–N_4 (M = Cr, Mn, Fe, Co, Cu) single-atom photocatalysts were developed for the photo-Fenton reaction,[191] among which Cr–N_4 is the most efficient toward removing gaseous bisphenol A under visible light irradiation in a wide pH window from 3.0 to 11.0 (Fig. 11d). The accelerated separation of photogenerated carriers and cycling of the Cr^{3+}/Cr^{2+} couple could be attributed to the cooperation of photocatalysis and single atom catalysis. DFT calculations verified that Cr–N_4 with a metalloporphyrin-like structure showed higher activity in decomposing H_2O_2 to produce ·OH. Au is another element that can trigger the photo-Fenton reaction. Han *et al.* found that Au@MoS_2 could produce H_2O_2 from H_2O and air under natural sunlight illumination, with H_2O_2 production rate (791.72 μM of H_2O_2 was produced in 6 hours) 2.5 times that of pure MoS_2 (Fig. 11e).[192] The researchers further used Mn^{2+} to boost H_2O_2 production by 2 times. These studies extended the photo-Fenton reaction to iron-free catalysts and offered new strategies to develop advanced gas purification techniques. Dual atom catalysts were also developed to further promote the photo-Fenton reaction activity. Niu *et al.* established an N,P-coordinated Ni, Fe dual-atom photocatalyst (CN-

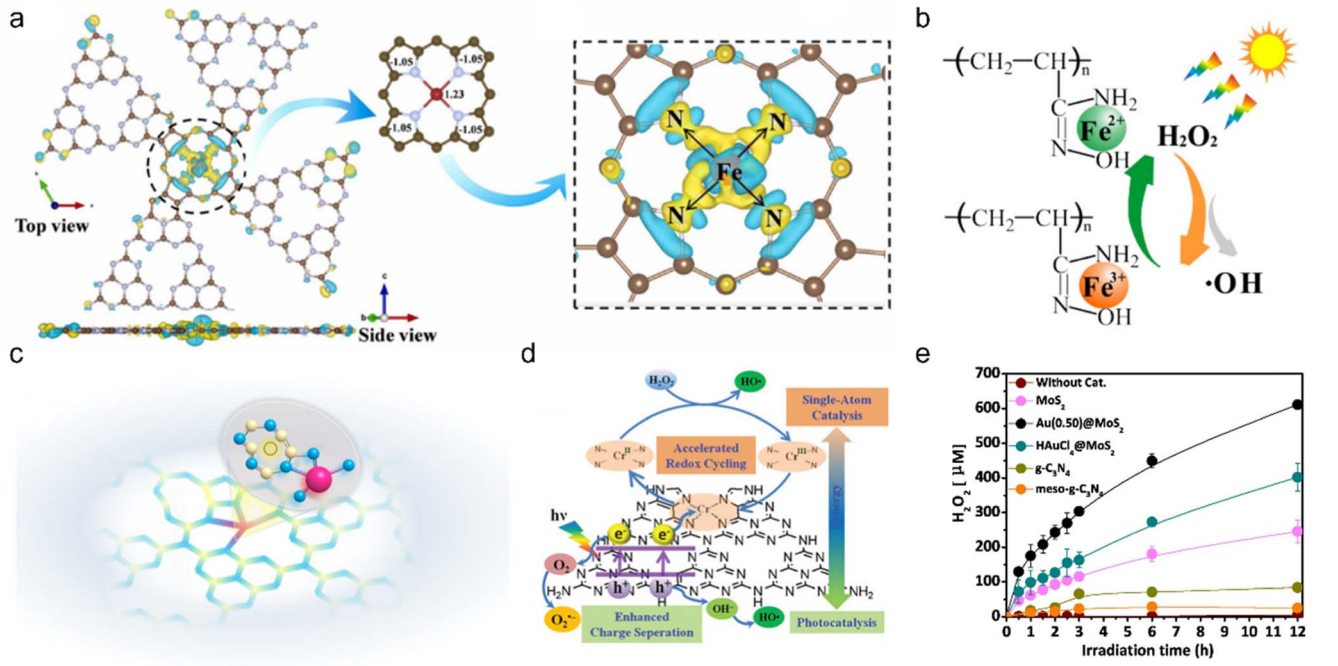

Fig. 11 (a) Bader charge and differential charge distribution analyses of pyrrolic-type FeN_4. Reproduced with permission from ref. 187 Copyright 2022, Elsevier. (b) Proposed photo-Fenton mechanism of U-g-PAO/Fe. Reproduced with permission from ref. 188 Copyright 2021, Elsevier. (c) Schematic model of Fe_1-N_v/CN, Fe (rose red), N (blue), C (yellow) and N vacancy (black dotted circle). Reproduced with permission from ref. 190 Copyright 2021, Wiley-VCH. (d) Schematic illustration showing synergy in SA-Cr/PN-g-C_3N_4 + H_2O_2 + Vis system for producing ·OH. Reaction conditions: [BPA] = 10 mg L^{-1}, [H_2O_2] = 165 μM, [Catalyst] = 0.2 g L^{-1}, and pH = 7.0. Reproduced with permission from ref. 191 Copyright 2021, Wiley-VCH. (e) Photocatalytic H_2O_2 production over various catalysts. Reaction conditions: 300 W Xe lamp, 0.05 g photocatalyst, 50 mL H_2O, pH = 5, 10 °C, ambient atmosphere. Reproduced with permission from ref. 192 Copyright 2019, Elsevier.

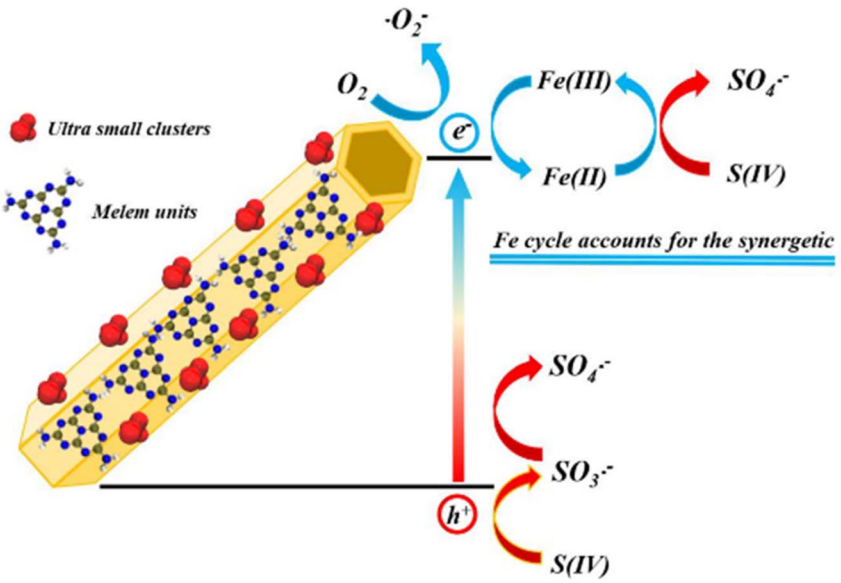

Fig. 12 Schematic illustration showing the mechanisms for S(IV) activation by MF2 under visible light irradiation. Reproduced with permission from ref. 194 Copyright 2021, Elsevier.

FeNi-P) to activate H_2O_2 under light irradiation.[193] DFT calculations found that the single-Ni-atom center functioned as the active site to produce ·OH. The strong interaction between Fe and Ni single atoms linked with a P-bridge could efficiently decrease ·OH formation energy. Therefore, CN-FeNi-P delivered an excellent gaseous moxifloxacin removal ability, 3.7 times that of pure CN. This study introduces a dual atom photocatalyst into the photo-Fenton reaction and opens a new window for designing novel atomically dispersed photocatalysts for environmental treatment.

4.2.3. Other reactions. Sulfite [S(IV)] activation provides another efficient method to degrade pollutants. Tong *et al.* fabricated single Fe atoms onto a bamboo-like porous g-C_3N_4 for S(IV) activation (Fig. 12).[194] The catalyst with 2.5 wt‰ Fe displayed 16 times higher S(IV) activation activity and diclofenac removal rate compared to pure g-C_3N_4 under visible light irradiation. The much-enhanced performance was attributed to the formation of an Fe–S(IV) complex. Detailed experiments revealed that the diclofenac removal process involved decarboxylation, hydroxylation, chlorine abstraction and cleavage at the bridging N atoms, consistent with the Fukui index prediction.

4.3 Electrocatalytic reactions

SAC-based electrocatalysis has shown powerful oxidation capability and has been extensively used for environmental treatment. Electrocatalysis alone can remove contaminated gas and deliver good performance. Integrating electrocatalysis with the PMS system or applying photoelectrocatalysis demonstrates stronger oxidation ability and thus achieves better contaminated gas removal performance.[195]

4.3.1. Electrocatalysis alone. Electrochemical reduction or oxidation works as a promising approach to remove contaminated gas due to the facile operation conditions and high efficiency.[196] Recently, electrocatalysis has garnered unprecedented attention in nitrogen-containing molecule upgradation, which enables conversion of nitrogen-containing waste into a wide range of high value-added chemicals under mild operating conditions, including NH_3, NH_2OH, N_2H_4, urea, and cyclohexanone oxime.[197–200] It represents an exemplary technical solution for transforming waste into valuable resources (Fig. 13a), which has attracted significant interest in the scientific community.[201] Fig. 13b shows the relationship between the calculated ΔG for NO adsorption on transition metal (TM)-N_4/graphene and the d-band center of the central TM, demonstrating a clear linear correlation.[202] For instance, when Fe, Co, and Cu atoms are individually incorporated into graphene, their computed d-band centers are approximately −2.97 eV, −3.19 eV, and −3.52 eV respectively. These values align well with their corresponding NO adsorption strengths (ΔG = −1.27 eV, −0.77 eV, and +0.06 eV). Therefore, it can be inferred that variations in ΔG values among different TM-N_4/graphene directly correspond to shifts in the position of the d-band center.[203,204] The moderate d-band center observed in Co-N_4/graphene results in a balanced interaction between its surface and adsorbed NO molecules, which accounts for enhanced kinetics in the NO reduction reaction (NORR) on Co-N_4/graphene. Chu *et al.* anchored single W atoms onto MoO_3 nanosheets (W_1/MoO_{3-x}) and studied its application in NO removal.[205] It was found that W_1/MoO_{3-x} not only delivered super performance towards NH_3 generation, but also displayed enhanced H_2O dissociation while suppressing *H dimerization to increase proton supply. In contrast to the weakly adsorbed NO on pristine MoO_3, the O_V-induced coordinatively unsaturated motifs of Mo_1–O_5 (in MoO_{3-x}) and W_1–O_5 (in W_1/MoO_{3-x}) exhibited remarkable NO adsorption capability with efficient dissociation of the N=O bond.[206] As a result, W_1/MoO_{3-x} exhibited outstanding catalytic performance in the NORR. Besides W, In SAs have also been extensively investigated for the

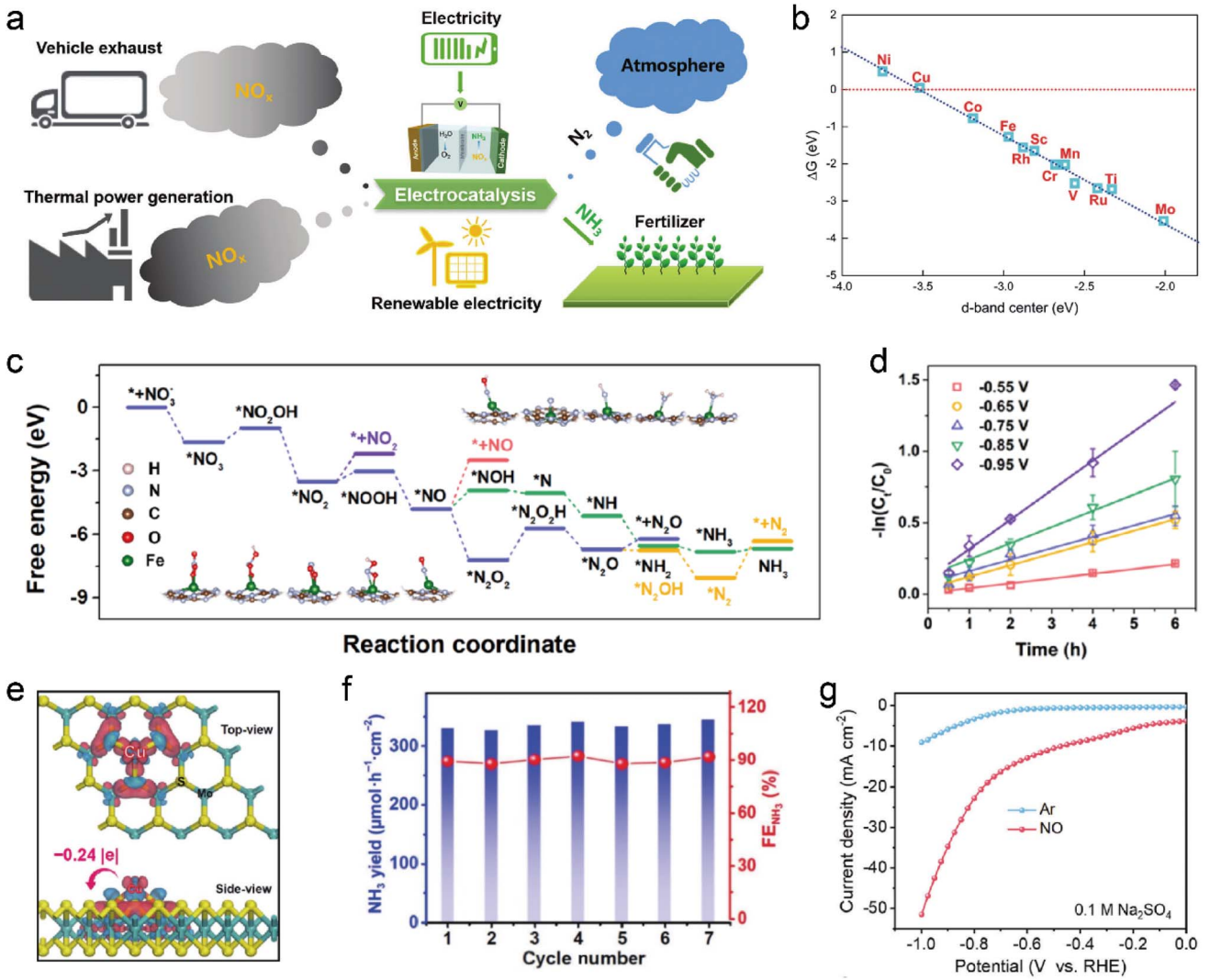

Fig. 13 (a) Schematic diagram of the electrocatalytic reduction of NO to NH_3. Reproduced with permission from ref. 201 Copyright 2023, Wiley-VCH. (b) Calculated NO adsorption free energy (ΔG) on TM-N_4/graphene *versus* the d-band center of the central TM atom. Reproduced with permission from ref. 202 Copyright 2018, Royal Society of Chemistry. (c) Free energy diagram of electrochemical NO_3^- reduction on Fe_1/g-C_3N_4. (d) Kinetic linear fitting for NO_3-N removal at different voltages. Reproduced with permission from ref. 208 Copyright 2022, Elsevier. (e) Charge density difference of the Cu_1–S_3 motif on MoS_2. Red and blue denote charge accumulation and depletion regions, respectively. (f) Cycling test of Cu_1/MoS_2 performed at −0.6 V *vs.* RHE. Reproduced with permission from ref. 209 Copyright 2022, Springer. (g) LSV curves of CuFe DS/NC measured in Ar and NO-saturated 0.1 M Na_2SO_4 in an H-type cell. Reproduced with permission from ref. 201 Copyright 2023, Wiley-VCH.

NORR. As reported by Chu and co-workers, the In SAs with an In_1–O_5 motif confined in amorphous MoO_3 achieved the highest NO reduction to ammonia faradaic efficiency (FE) of 85% with an NH_3 yield rate of 0.29 mmol h^{-1} cm^{-2}.[207] The N–N coupling was effectively prevented over the as-developed In SAC due to lack of continuous active sites, which suppressed N_2 production and improved ammonia selectivity. Li *et al.* reported that a NO-preoccupied transition state would occur on the single-Fe-atom site, which would limit water adsorption and the HER, leading to an outstanding nitrate reduction to ammonia performance with an ammonia yield rate of 30 mol h^{-1} g_{Fe}^{-1} and an ultrahigh ammonia FE of 100% (Fig. 13c–d).[208] Besides, Cu single atoms were also scrutinized. DFT calculations showed a noticeable electronic interaction in the Cu–S_3 motif having −0.24|*e*| electron transfer from the Cu single atom to the surrounding S atoms (Fig. 13e).[209] As a result, CuS_3 could produce ammonia at a rate of 0.34 mmol h^{-1} cm^{-2} in the NORR (Fig. 13f). Additionally, dual-atom catalysts (*e.g.*, CuFe DS/NC) also exhibited remarkable efficacy in NO reduction to produce NH_3 (Fig. 13g).[201]

4.3.2. Electrochemical activation of peroxymonosulfate (electro-PMS). Electrochemical activation of peroxymonosulfate (electro-PMS) emerges as a promising method for environmental remediation because $\cdot SO_4^-$ has a stronger oxidation ability and a longer half-life (2.5–3.1 V *vs.* NHE, 30–40 μs) than ·OH (1.8–2.7 V *vs.* NHE, 20 ns),[210,211] which can be operated in a wide pH window from 2 to 8. Liu *et al.* deposited Fe SAs onto $Mo_2TiC_2T_x$ MXene with abundant Mo vacancies (Fe-SA/

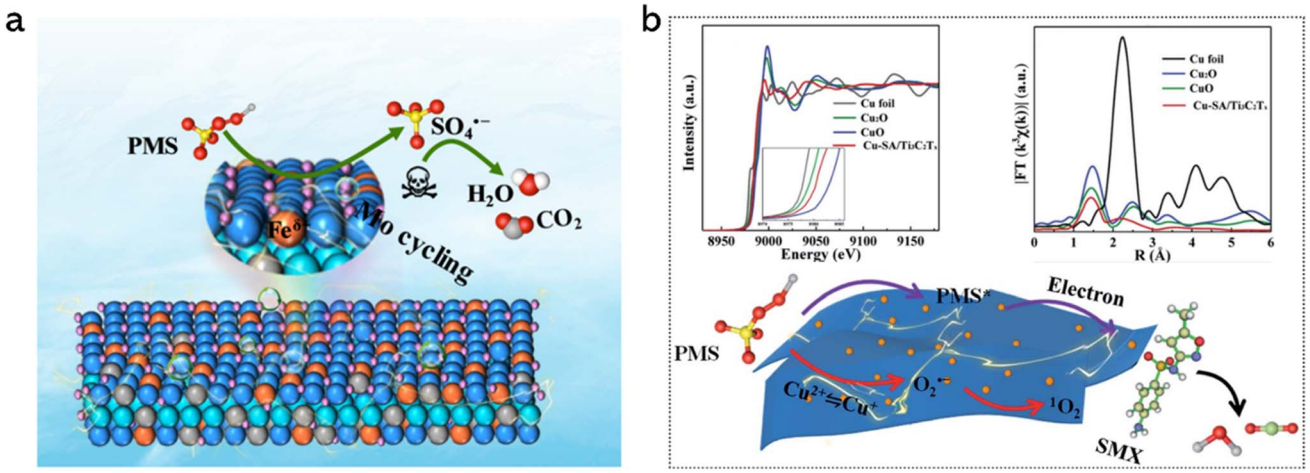

Fig. 14 (a) Proposed mechanism of electro-PMS activation for SMX degradation over Fe-SA/$Mo_2TiC_2T_x$. Reproduced with permission from ref. 212 Copyright 2022, American Chemical Society. (b) Top left: XANES spectra at the Cu K-edge. Top right: the k^2-weighted Fourier transformed EXAFS spectra, where $\chi(k)$ denotes the EXAFS oscillation function. Bottom: schematic illustration showing the proposed electro-PMS activation mechanism on the Cu-SA/$Ti_3C_2T_x$ filter. Reproduced with permission from ref. 213 Copyright 2021, Royal Society of Chemistry.

$Mo_2TiC_2T_x$) for PMS activation (Fig. 14a).[212] The Mo vacancies not only provided sites to anchor Fe atoms *via* forming Fe–O bonds, but also served as the co-catalyst to prompt a Fenton-like reaction. The Fe-SA/$Mo_2TiC_2T_x$ catalyst could completely remove gaseous sulfamethoxazole (SMX) in a single-pass mode. It is worth mentioning that the SMX degradation activity showed a 24-fold and 67-fold increase over Fe-SA/$Mo_2TiC_2T_x$ as compared to that over Fe-NP/$Mo_2TiC_2T_x$ and pure $Mo_2TiC_2T_x$. Experimental studies and DFT calculations revealed that the single-atom Fe sites were responsible for the adsorption and activation of PMS to generate reactive $SO_4^{\cdot-}$ under an electric field. Liu *et al.* fabricated Cu-SA/$Ti_3C_2T_x$ with a $Cu–O_3$ coordination for PMS activation to remove SMX (Fig. 14b).[213] It was found that $^1O_2$ was the main active species generated over Cu-SA/$Ti_3C_2T_x$, while ·OH was the dominant species generated over Cu-NP/$Ti_3C_2T_x$, responsible for SMX degradation, indicating the importance of size effect in PMS activation.

4.3.3. Photoelectrocatalysis (PEC). PEC provides another powerful method for addressing environmental issues.[214–216] Zhao *et al.* used Cu-SA/TiO_{2-x} to selectively reduce O_2 to H_2O_2 in a wide pH range (7–11).[217] The H_2O_2 concentration could reach 276.23 μmol L^{-1} at pH = 9 (Fig. 15a), and 96.3% of sulfamethoxazole could be degraded over Cu-SA/TiO_{2-x} within 10 min. The catalyst also demonstrated excellent performance in five other wastewater samples, indicating the wide application potential of the developed catalyst for wastewater treatment. Zhao *et al.* deposited Pd SAs onto F–TiO_2 with a Pd–F_4O_2 coordination to selectively reduce O_2 to H_2O_2 with a selectivity up to 99% (Fig. 15b).[218] Note that an additional channel bond HO–O···Pd–F-TiO_2 propelled electron migration from the

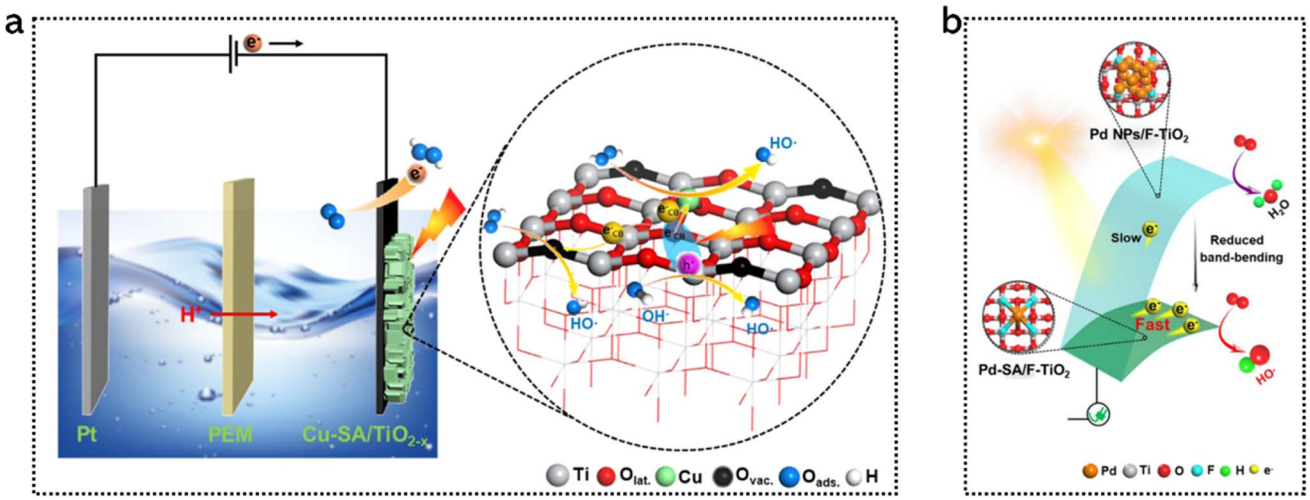

Fig. 15 (a) Schematic diagram showing photoelectrocatalytic oxygen reduction on the $Cu_{0.46}$-SA/TiO_{2-x} photocathode in an alkaline solution. Reproduced with permission from ref. 217 Copyright 2022, American Chemical Society. (b) Mechanism for photoelectrocatalytic O_2 reduction to HO· over Pd-SA/F-TiO_2 and Pd NPs/F-TiO_2. Reproduced with permission from ref. 218 Copyright 2022, American Chemical Society.

conduction band of F-TiO_2 to Pd SAs to reduce Pd···O–OH to ·OH. The ·OH generation rate could reach 9.18 μmol L^{-1} min^{-1}, one order of magnitude higher than that in conventional advanced oxidation processes reported in the literature. As a result, the kinetics of BPA and acetaminophen degradation reached as high as 0.324 min^{-1} and 0.175 min^{-1}, respectively, and 93.2% of total organic carbon and 99.3% of toxicity could be removed in 60 min. Through PEC, organic pollutants can even be upgraded to value-added products. Qu *et al.* developed single Ru atoms on Cu_2O to degrade organics,[219] which achieved almost complete removal of BPA (99.6%). More importantly, NH_3 could be produced concurrently (yield: ~37.4 μg h^{-1} mg_{cat}^{-1}, FE: ~17.1%) at low voltages. The whole system could decrease energy consumption by ~51.8% compared to the nitrogen reduction reaction (NRR) process.

5. Summary and outlook

In this review, we first provided a concise introduction to the significance and urgency of gas detection and pollutant purification, followed by a comprehensive overview of the structural feature identification methods for SACs. Subsequently, the recent advances of SACs used in environmental detection and remediation were systematically elaborated. Although great efforts have been made in developing SACs for environmental applications, many issues still remain. Next, we are going to propose some solutions to address the current challenges and expedite the development of SACs in pollution gas detection and purification (Fig. 16). The development of advanced synthesis techniques enables more precise control over the size, shape, and distribution of individual atoms on the support material, thereby facilitating optimization of catalytic activity and selectivity in SACs. The utilization of model small molecules for immobilization aids in the creation of model SAC systems, which can offer valuable insights into the structure and behavior of SACs, aid in design optimization and performance prediction for gas sensing applications. In SACs, equal attention should be given to understanding the specific role played by the support materials; however, this aspect is often overlooked in current research. Future investigations shall focus on comprehending how support materials influence monatomic behavior and exploring modifications that can enhance SAC performance. Furthermore, machine learning and artificial intelligence can be employed to predict the structure, composition, and performance of SACs. A comprehensive study on the response pathway of SACs can provide significant insights into their sensing mechanisms, enabling the design of highly selective and sensitive SACs. Additionally, developing environmentally friendly SACs using non-toxic elements represents an important strategy contributing to sustainable development. These strategies have immense potential to revolutionize the field of SACs while opening up new opportunities for their applications in gas sensing and other domains.

(1) Structural homogenization for SACs: most of the SACs are prepared *via* high-temperature pyrolysis, consequently, it is difficult to construct SACs with a precise coordination environment. Nowadays, only EXAFS measurement can be utilized to probe the local structure of SACs. However, EXAFS can only provide the average structure rather than the local structure information. Furthermore, EXAFS cannot distinguish M–N, M–C and M–O bonds due to the similar atomic weight of N, C and O atoms. Even if the coordination numbers are the same, the

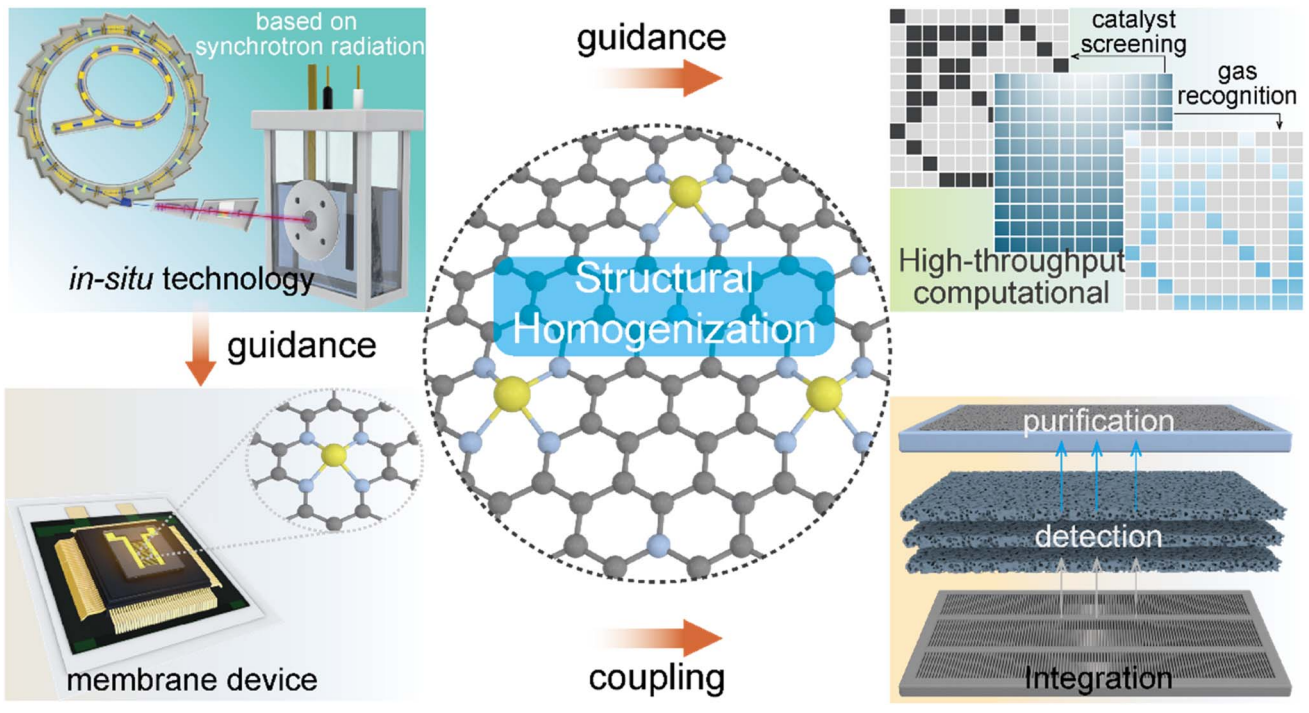

Fig. 16 The outlook diagram highlighting the future research directions.

moieties can be located on the plane, at the edge, or coordinated with another vacancy. The above-mentioned factors lead to the controversy over the coordination structure of SACs. Without the precise local structure, the subsequent mechanism exploration and explanation based on the electronic states of the single metal atoms will become less meaningful. Synthesizing SACs at low temperature or even at room temperature may provide a guarantee for the development of SACs with a uniform structure.

(2) Novel SAC design: although SACs have been extensively used for environmental application, the working mechanism of SACs is still unclear because of the complex multiple electron-transfer steps. Determining the underlying working principle that governs the performance in environmental remediation is conducive to the rapid exploitation of novel efficient SACs. Employing *in situ* techniques, such as *in situ* XAS and *in situ* XPS, serves as a promising route to probe the structural evolution and the reaction pathway under working conditions.[38,220] Also, designing dual atom catalysts based on the understanding of SACs is beneficial to further improve the catalyst's activity and stability.[221]

(3) High-throughput computational screening of SACs: the conventional catalyst development process heavily relying on experiments cannot meet the industrial requirements. Using DFT predictions and deploying machine learning methods for high-throughput screening can speed up catalyst design and development process to obtain promising self-powered sensing platforms for future hyperscaling of the Internet of Things systems.[222] Moreover, SACs are now utilized to remove pollutants in the lab scale; scale-up experiments in a real environment, such as rivers or seas, are highly needed.

(4) Membrane device based on SACs: SACs are typically prepared in the powder form before being deposited onto a membrane for gas detection or pollutant degradation purposes. However, there exists a significant disparity between the activity of SACs and the performance in real devices incorporating SACs, resulting in unsatisfactory practical applications. Therefore, directly constructing SACs onto a membrane as a monolithic catalyst can ensure the high activity of SACs and propel the commercialization of SAC-based gas sensors and other related products.

(5) Integration of detection and purification of contaminated gas: at the current stage of study, environmental detection and remediation are conducted as separate processes. Considering the exceptional monitoring and remediation capabilities of SACs, integrating them into a single device with both detection and remediation functionalities will become a focal point for future research.

Author contributions

All of the authors contributed to the literature search, writing and editing of this review.

Conflicts of interest

There are no conflicts to declare.

Acknowledgements

This work was supported by the City University of Hong Kong startup fund (9020003), ITF – RTH – Global STEM Professorship (9446006), the ECF 88/2021 and PolyU Project of Strategic Importance (1-ZE2W) for Funding, the National Natural Science Foundation of China (No. 21976086, Grant No. 22075195), and the National Key Research and Development Program of China (No. 2019YFC1804201).

References

1 D. J. Wales, J. Grand, V. P. Ting, R. D. Burke, K. J. Edler, C. R. Bowen, S. Mintova and A. D. Burrows, Gas sensing using porous materials for automotive applications, *Chem. Soc. Rev.*, 2015, **44**, 4290–4321.
2 J. Liu, L. Zhang, J. Fan and J. Yu, Semiconductor gas sensor for triethylamine detection, *Small*, 2022, **18**, 2104984.
3 L. J. Carter, Uncontrolled SO_2 emissions bring acid rain, *Science*, 1979, **204**, 1179.
4 M. Cipolla, M. Sorgenti, C. Gentile and M. M. Bishara, in *Clinical Handbook of Air Pollution-Related Diseases*, ed. F. Capello and A. V. Gaddi, Springer International Publishing, Cham, 2018, pp. 327–339, DOI: 10.1007/978-3-319-62731-1_18.
5 T. Becker, S. Mühlberger, C. B.-v. Braunmühl, G. Müller, T. Ziemann and K. V. Hechtenberg, Air pollution monitoring using tin-oxide-based microreactor systems, *Sens. Actuators, B*, 2000, **69**, 108–119.
6 A. Wang, J. Li and T. Zhang, Heterogeneous single-atom catalysis, *Nat. Rev. Chem*, 2018, **2**, 65–81.
7 X. Li, H. Rong, J. Zhang, D. Wang and Y. Li, Modulating the local coordination environment of single-atom catalysts for enhanced catalytic performance, *Nano Res.*, 2020, **13**, 1842–1855.
8 X. N. Li, Y. Q. Huang and B. Liu, Catalyst: single-atom catalysis: directing the way toward the nature of catalysis, *Chem*, 2019, **5**, 2733–2735.
9 J.-X. Liang, Y.-G. Wang, X.-F. Yang, D.-H. Xing, A.-Q. Wang, T. Zhang and J. Li, in *Encyclopedia of Inorganic and Bioinorganic Chemistry*, 2017, pp. 1–11.
10 B. Lu, Q. Liu and S. Chen, Electrocatalysis of single-atom sites: Impacts of atomic coordination, *ACS Catal.*, 2020, **10**, 7584–7618.
11 B. Han, Y. Guo, Y. Huang, W. Xi, J. Xu, J. Luo, H. Qi, Y. Ren, X. Liu, B. Qiao and T. Zhang, Strong metal-support interactions between Pt single atoms and TiO_2, *Angew. Chem., Int. Ed.*, 2020, **59**, 11824–11829.
12 X.-F. Yang, A. Wang, B. Qiao, J. Li, J. Liu and T. Zhang, Single-atom catalysts: A new frontier in heterogeneous catalysis, *Acc. Chem. Res.*, 2013, **46**, 1740–1748.
13 H. B. Yang, S.-F. Hung, S. Liu, K. Yuan, S. Miao, L. Zhang, X. Huang, H.-Y. Wang, W. Cai, R. Chen, J. Gao, X. Yang, W. Chen, Y. Huang, H. M. Chen, C. M. Li, T. Zhang and B. Liu, Atomically dispersed Ni(i) as the active site for electrochemical CO_2 reduction, *Nat. Energy*, 2018, **3**, 140–147.

14 X. Liang, N. Fu, S. Yao, Z. Li and Y. Li, The progress and outlook of metal single-atom-site catalysis, *J. Am. Chem. Soc.*, 2022, **144**, 18155–18174.
15 J. Ding, Z. Wei, F. Li, J. Zhang, Q. Zhang, J. Zhou, W. Wang, Y. Liu, Z. Zhang, X. Su, R. Yang, W. Liu, C. Su, H. B. Yang, Y. Huang, Y. Zhai and B. Liu, Atomic high-spin cobalt(II) center for highly selective electrochemical CO reduction to CH_3OH, *Nat. Commun.*, 2023, **14**, 6550.
16 X. Li, X. Yang, Y. Huang, T. Zhang and B. Liu, Supported noble-metal single atoms for heterogeneous catalysis, *Adv. Mater.*, 2019, **31**, 1902031.
17 G. Lei, H. Pan, H. Mei, X. Liu, G. Lu, C. Lou, Z. Li and J. Zhang, Emerging single atom catalysts in gas sensors, *Chem. Soc. Rev.*, 2022, **51**, 7260–7280.
18 M. Zhang, G. Wang, J. Chen and X. Lu, Single atom catalysts for sensors, *Trends Anal. Chem.*, 2023, **169**, 117399.
19 Z. Li, E. Tian, S. Wang, M. Ye, S. Li, Z. Wang, Z. Ma, G. Jiang, C. Tang, K. Liu and J. Jiang, Single-atom catalysts: promotors of highly sensitive and selective sensors, *Chem. Soc. Rev.*, 2023, **52**, 5088–5134.
20 J. Zeng, Q. Rong, B. Xiao, R. Yu, B. Zi, X. Kuang, X. Deng, Y. Ma, J. Zhang, J. Wu and Q. Liu, Single-atom silver loaded on tungsten oxide with oxygen vacancies for high performance triethylamine gas sensors, *J. Mater. Chem. A*, 2021, **9**, 8704.
21 J. Qiu, X. Hu, L. Shi, J. Fan, X. Min, W. Zhang and J. Wang, Enabling selective, room-temperature gas detection using atomically dispersed Zn, *Sens. Actuators, B*, 2021, **329**, 129221.
22 R. Tian, P. Ji, Z. Luo, J. Li and J. Sun, Room-temperature NH_3 gas sensor based on atomically dispersed Co with a simple structure, *New J. Chem.*, 2021, **45**, 10240–10247.
23 T. Chu, C. Rong, L. Zhou, X. Mao, B. Zhang and F. Xuan, Progress and perspectives of single-atom catalysts for gas sensing, *Adv. Mater.*, 2023, **35**, e2206783.
24 M. Wang, M. Ye, J. Wang, Y. Xu, Z. Wang, X. Tong, X. Han, K. Zhang, W. Wang, K. Wu and X. Wei, Recent advances and applications of single atom catalysts based electrochemical sensors, *Nano Res.*, 2024, **17**, 2993–3013.
25 F. Gu, C. Luo, D. Han, S. Hong and Z. Wang, Atomically dispersed Pt on 3DOM WO_3 promoted with cobalt and nickel oxides for highly selective and highly sensitive detection of xylene, *Sens. Actuators, B*, 2019, **297**, 126772.
26 T. Cai, Z. Teng, Y. Wen, H. Zhang, S. Wang, X. Fu, L. Song, M. Li, J. Lv and Q. Zeng, Single-atom site catalysts for environmental remediation: Recent advances, *J. Hazard. Mater.*, 2022, **440**, 129772.
27 Y. Shang, X. Xu, B. Gao, S. Wang and X. Duan, Single-atom catalysis in advanced oxidation processes for environmental remediation, *Chem. Soc. Rev.*, 2021, **50**, 5281–5322.
28 L. Zhang, Y. Ren, W. Liu, A. Wang and T. Zhang, Single-atom catalyst: a rising star for green synthesis of fine chemicals, *Natl. Sci. Rev.*, 2018, **5**, 653–672.
29 R. Xie, K. Guo, Z. Ao, Z. Suo, H. Huang and D. Y. C. Leung, Surface-bound radicals generated from cobalt single-atom catalyst: Mechanism of boosting Fenton-like reactions, *Chem. Eng. J.*, 2023, **461**, 141920.
30 Q. Li, Z. Li, Q. Zhang, L. Zheng, W. Yan, X. Liang, L. Gu, C. Chen, D. Wang, Q. Peng and Y. Li, Porous γ-Fe_2O_3 nanoparticle decorated with atomically dispersed platinum: study on atomic site structural change and gas sensor activity evolution, *Nano Res.*, 2020, **14**, 1435–1442.
31 S. Lv, H. Wang, Y. Zhou, D. Tang and S. Bi, Recent advances in heterogeneous single-atom nanomaterials: From engineered metal-support interaction to applications in sensors, *Coord. Chem. Rev.*, 2023, **478**, 214976.
32 J. Ding, J. Huang, Q. Zhang, Z. Wei, Q. He, Z. Chen, Y. Liu, X. Su and Y. Zhai, A hierarchical monolithic cobalt-single-atom electrode for efficient hydrogen peroxide production in acid, *Catal. Sci. Technol.*, 2022, **12**, 2416–2419.
33 J. Gao, H. b. Yang, X. Huang, S.-F. Hung, W. Cai, C. Jia, S. Miao, H. M. Chen, X. Yang, Y. Huang, T. Zhang and B. Liu, Enabling direct H_2O_2 production in acidic media through rational design of transition metal single atom catalyst, *Chem*, 2020, **6**, 658–674.
34 S. Liu, H. B. Yang, S. F. Hung, J. Ding, W. Cai, L. Liu, J. Gao, X. Li, X. Ren, Z. Kuang, Y. Huang, T. Zhang and B. Liu, Elucidating the electrocatalytic CO_2 reduction reaction over a model single-atom nickel catalyst, *Angew. Chem., Int. Ed.*, 2020, **59**, 798–803.
35 W. Liu, L. Zhang, X. Liu, X. Liu, X. Yang, S. Miao, W. Wang, A. Wang and T. Zhang, Discriminating catalytically active FeN_x species of atomically dispersed Fe–N–C catalyst for selective oxidation of the C–H bond, *J. Am. Chem. Soc.*, 2017, **139**, 10790–10798.
36 F. Chen, X. Jiang, L. Zhang, R. Lang and B. Qiao, Single-atom catalysis: Bridging the homo- and heterogeneous catalysis, *Chin. J. Catal.*, 2018, **39**, 893–898.
37 N. Cheng, L. Zhang, K. Doyle-Davis and X. Sun, Single-atom catalysts: From design to application, *Electrochem. Energy Rev.*, 2019, **2**, 539–573.
38 X. Li, X. Yang, J. Zhang, Y. Huang and B. Liu, *In situ/operando* techniques for characterization of single-atom catalysts, *ACS Catal.*, 2019, **9**, 2521–2531.
39 Y. Liu, J. Ding, F. Li, X. Su, Q. Zhang, G. Guan, F. Hu, J. Zhang, Q. Wang, Y. Jiang, B. Liu and H. B. Yang, Modulating hydrogen adsorption via charge transfer at the semiconductor–metal heterointerface for highly efficient hydrogen evolution catalysis, *Adv. Mater.*, 2022, **35**, 2207114.
40 Y. Liu, Q. Wang, J. Zhang, J. Ding, Y. Cheng, T. Wang, J. Li, F. Hu, H. B. Yang and B. Liu, Recent advances in carbon-supported noble-metal electrocatalysts for hydrogen evolution reaction: syntheses, structures, and properties, *Adv. Energy Mater.*, 2022, **12**, 2200928.
41 J. Yang, H. Qi, A. Li, X. Liu, X. Yang, S. Zhang, Q. Zhao, Q. Jiang, Y. Su, L. Zhang, J. F. Li, Z. Q. Tian, W. Liu, A. Wang and T. Zhang, Potential-driven restructuring of Cu single atoms to nanoparticles for boosting the electrochemical reduction of nitrate to ammonia, *J. Am. Chem. Soc.*, 2022, **144**, 12062–12071.

42 R. Qin, K. Liu, Q. Wu and N. Zheng, Surface coordination chemistry of atomically dispersed metal catalysts, *Chem. Rev.*, 2020, **120**, 11810–11899.
43 J. Yang, W. Liu, M. Xu, X. Liu, H. Qi, L. Zhang, X. Yang, S. Niu, D. Zhou, Y. Liu, Y. Su, J. F. Li, Z. Q. Tian, W. Zhou, A. Wang and T. Zhang, Dynamic behavior of single-atom catalysts in electrocatalysis: identification of Cu-N_3 as an active site for the oxygen reduction reaction, *J. Am. Chem. Soc.*, 2021, **143**, 14530–14539.
44 Y. Zeng, J. Zhao, S. Wang, X. Ren, Y. Tan, Y. R. Lu, S. Xi, J. Wang, F. Jaouen, X. Li, Y. Huang, T. Zhang and B. Liu, Unraveling the electronic structure and dynamics of the atomically dispersed iron sites in electrochemical CO_2 reduction, *J. Am. Chem. Soc.*, 2023, **145**, 15600–15610.
45 H. Qi, J. Yang, F. Liu, L. Zhang, J. Yang, X. Liu, L. Li, Y. Su, Y. Liu, R. Hao, A. Wang and T. Zhang, Highly selective and robust single-atom catalyst Ru_1/NC for reductive amination of aldehydes/ketones, *Nat. Commun.*, 2021, **12**, 3295.
46 X. Ren, S. Liu, H. Li, J. Ding, L. Liu, Z. Kuang, L. Li, H. Yang, F. Bai, Y. Huang, T. Zhang and B. Liu, Electron-withdrawing functional ligand promotes CO_2 reduction catalysis in single atom catalyst, *Sci. China Chem.*, 2020, **63**, 1727–1733.
47 Y. J. Ren, Y. Tang, L. L. Zhang, X. Y. Liu, L. Li, S. Miao, D. S. Su, A. Q. Wang, J. Li and T. Zhang, Unraveling the coordination structure-performance relationship in Pt_1/Fe_2O_3 single-atom catalyst, *Nat. Commun.*, 2019, **10**, 4500.
48 X. Z. Shao, X. F. Yang, J. M. Xu, S. Liu, S. Miao, X. Y. Liu, X. Su, H. M. Duan, Y. Q. Huang and T. Zhang, Iridium single-atom catalyst performing a quasi-homogeneous hydrogenation transformation of CO_2 to formate, *Chem*, 2019, **5**, 693–705.
49 B. T. Qiao, A. Q. Wang, X. F. Yang, L. F. Allard, Z. Jiang, Y. T. Cui, J. Y. Liu, J. Li and T. Zhang, Single-atom catalysis of CO oxidation using Pt_1/FeO_x, *Nat. Chem.*, 2011, **3**, 634–641.
50 R. Lang, T. Li, D. Matsumura, S. Miao, Y. Ren, Y.-T. Cui, Y. Tan, B. Qiao, L. Li, A. Wang, X. Wang and T. Zhang, Hydroformylation of olefins by a rhodium single-atom catalyst with activity comparable to $RhCl(PPh_3)_3$, *Angew. Chem., Int. Ed.*, 2016, **55**, 16054–16058.
51 X. Su, X.-F. Yang, Y. Huang, B. Liu and T. Zhang, Single-atom catalysis toward efficient CO_2 conversion to CO and formate products, *Acc. Chem. Res.*, 2019, **52**, 656–664.
52 Z. Chen, H. Niu, J. Ding, H. Liu, P. H. Chen, Y. H. Lu, Y. R. Lu, W. Zuo, L. Han, Y. Guo, S. F. Hung and Y. Zhai, Unraveling the origin of sulfur-doped Fe-N-C single-atom catalyst for enhanced oxygen reduction activity: effect of iron spin-state tuning, *Angew. Chem., Int. Ed.*, 2021, **60**, 25404–25410.
53 L. Liu, T. Xiao, H. Fu, Z. Chen, X. Qu and S. Zheng, Construction and identification of highly active single-atom Fe_1-NC catalytic site for electrocatalytic nitrate reduction, *Appl. Catal., B*, 2023, **323**, 122181.
54 L. Fang, S. Seifert, R. E. Winans and T. Li, *Operando* XAS/SAXS: Guiding design of single-atom and subnanocluster catalysts, *Small Methods*, 2021, **5**, 2001194.
55 S. Qiao, Q. He, P. Zhang, Y. Zhou, S. Chen, L. Song and S. Wei, Synchrotron-radiation spectroscopic identification towards diverse local environments of single-atom catalysts, *J. Mater. Chem. A*, 2022, **10**, 5771–5791.
56 X. Li, C.-S. Cao, S.-F. Hung, Y.-R. Lu, W. Cai, A. I. Rykov, S. Miao, S. Xi, H. Yang, Z. Hu, J. Wang, J. Zhao, E. E. Alp, W. Xu, T.-S. Chan, H. Chen, Q. Xiong, H. Xiao, Y. Huang, J. Li, T. Zhang and B. Liu, Identification of the electronic and structural dynamics of catalytic centers in single-Fe-atom material, *Chem*, 2020, **6**, 3440–3454.
57 S. Das and V. Jayaraman, SnO_2: A comprehensive review on structures and gas sensors, *Prog. Mater. Sci.*, 2014, **66**, 112–255.
58 W. Y. Chen, X. Jiang, S.-N. Lai, D. Peroulis and L. Stanciu, Nanohybrids of a MXene and transition metal dichalcogenide for selective detection of volatile organic compounds, *Nat. Commun.*, 2020, **11**, 1302.
59 J. Liu, L. Zhang, J. Fan, B. Zhu and J. Yu, Triethylamine gas sensor based on Pt-functionalized hierarchical ZnO microspheres, *Sens. Actuators, B*, 2021, **331**, 129425.
60 W. Yang, L. Feng, S. He, L. Liu and S. Liu, Density gradient strategy for preparation of broken In_2O_3 microtubes with remarkably selective detection of triethylamine vapor, *ACS Appl. Mater. Interfaces*, 2018, **10**, 27131–27140.
61 Y.-M. Jo, Y. K. Jo, J.-H. Lee, H. W. Jang, I.-S. Hwang and D. J. Yoo, MOF-based chemiresistive gas sensors: Toward new functionalities, *Adv. Mater.*, 2023, **35**, 2206842.
62 T. Lin, X. Lv, Z. Hu, A. Xu and C. Feng, Semiconductor metal oxides as chemoresistive sensors for detecting volatile organic compounds, *Sensors*, 2019, **19**, 233.
63 A. Marikutsa, M. Rumyantseva, E. A. Konstantinova and A. Gaskov, The key role of active sites in the development of selective metal oxide sensor materials, *Sensors*, 2021, **21**, 2554.
64 C. Wang, L. Yin, L. Zhang, D. Xiang and R. Gao, Metal oxide gas sensors: sensitivity and influencing factors, *Sensors*, 2010, **10**, 2088–2106.
65 R. Paul, B. Das and R. Ghosh, Novel approaches towards design of metal oxide based hetero-structures for room temperature gas sensor and its sensing mechanism: A recent progress, *J. Alloys Compd.*, 2023, **941**, 168943.
66 H. Ji, W. Zeng and Y. Li, Gas sensing mechanisms of metal oxide semiconductors: a focus review, *Nanoscale*, 2019, **11**, 22664–22684.
67 A. Dey, Semiconductor metal oxide gas sensors: A review, *J. Mater. Sci. Eng. B*, 2018, **229**, 206–217.
68 C. C. Li, Z. F. Du, L. M. Li, H. C. Yu, Q. Wan and T. H. Wang, Surface-depletion controlled gas sensing of ZnO nanorods grown at room temperature, *Appl. Phys. Lett.*, 2007, **91**, 032101.
69 L. Y. Zhu, L. X. Ou, L. W. Mao, X. Y. Wu, Y. P. Liu and H. L. Lu, Advances in noble metal-decorated metal oxide nanomaterials for chemiresistive gas sensors: Overview, *Nano-Micro Lett.*, 2023, **15**, 89.
70 W.-T. Koo, S.-J. Choi, S.-J. Kim, J.-S. Jang, H. L. Tuller and I.-D. Kim, Heterogeneous sensitization of metal–organic framework driven metal@metal oxide complex catalysts

on an oxide nanofiber scaffold toward superior gas sensors, *J. Am. Chem. Soc.*, 2016, **138**, 13431–13437.

71 P. Wang, T. Dong, C. Jia and P. Yang, Ultraselective acetone-gas sensor based ZnO flowers functionalized by Au nanoparticle loading on certain facet, *Sens. Actuators, B*, 2019, **288**, 1–11.

72 Y. Xu, L. Zheng, C. Yang, W. Zheng, X. Liu and J. Zhang, Oxygen vacancies enabled porous SnO_2 thin films for highly sensitive detection of triethylamine at room temperature, *ACS Appl. Mater. Interfaces*, 2020, **12**, 20704–20713.

73 V. Kumar, S. M. Majhi, K.-H. Kim, H. W. Kim and E. E. Kwon, Advances in In_2O_3-based materials for the development of hydrogen sulfide sensors, *Chem. Eng. J.*, 2021, **404**, 126472.

74 S. Uma and M. K. Shobana, Metal oxide semiconductor gas sensors in clinical diagnosis and environmental monitoring, *Sens. Actuators, A*, 2023, **349**, 114044.

75 P. Cao, Y. Cai, D. Pawar, S. T. Navale, C. N. Rao, S. Han, W. Xu, M. Fang, X. Liu, Y. Zeng, W. Liu, D. Zhu and Y. Lu, Down to ppb level NO_2 detection by ZnO/rGO heterojunction based chemiresistive sensors, *Chem. Eng. J.*, 2020, **401**, 125491.

76 L. Zheng, J. Xie, X. Liu, C. Yang, W. Zheng and J. Zhang, Unveiling the electronic interaction in ZnO/PtO/Pt nanoarrays for catalytic detection of triethylamine with ultrahigh sensitivity, *ACS Appl. Mater. Interfaces*, 2020, **12**, 46267–46276.

77 K. Sun, G. Zhan, L. Zhang, Z. Wang and S. Lin, Highly sensitive NO_2 gas sensor based on ZnO nanoarray modulated by oxygen vacancy with Ce doping, *Sens. Actuators, B*, 2023, **379**, 133294.

78 L. Liu and S. Liu, Oxygen vacancies as an efficient strategy for promotion of low concentration SO_2 gas sensing: the case of Au-modified SnO_2, *ACS Sustain. Chem. Eng.*, 2018, **6**, 13427–13434.

79 Y. Gui, K. Tian, J. Liu, L. Yang, H. Zhang and Y. Wang, Superior triethylamine detection at room temperature by {-112} faceted WO_3 gas sensor, *J. Hazard. Mater.*, 2019, **380**, 120876.

80 L. Liu, S. Shu, G. Zhang and S. Liu, Highly selective sensing of C_2H_6O, HCHO, and C_3H_6O gases by controlling SnO_2 nanoparticle vacancies, *ACS Appl. Nano Mater.*, 2018, **1**, 31–37.

81 K. G. Krishna, G. Umadevi, S. Parne and N. Pothukanuri, Zinc oxide based gas sensors and their derivatives: a critical review, *J. Mater. Chem. C*, 2023, **11**, 3906–3925.

82 Q. A. Drmosh, Y. A. Al Wajih, I. O. Alade, A. K. Mohamedkhair, M. Qamar, A. S. Hakeem and Z. H. Yamani, Engineering the depletion layer of Au-modified ZnO/Ag core-shell films for high-performance acetone gas sensing, *Sens. Actuators, B*, 2021, **338**, 129851.

83 H. J. Kim and J. H. Lee, Highly sensitive and selective gas sensors using p-type oxide semiconductors: Overview, *Sens. Actuators, B*, 2014, **192**, 607–627.

84 T. W. Yuan, Z. J. Li, W. S. Zhang, Z. G. Xue, X. Q. Wang, Z. H. Ma, Y. Fan, J. Q. Xu and Y. E. Wu, Highly sensitive ethanol gas sensor based on ultrathin nanosheets assembled Bi_2WO_6 with composite phase, *Sci. Bull.*, 2019, **64**, 595–602.

85 S. M. Majhi, A. Mirzaei, H. W. Kim, S. S. Kim and T. W. Kim, Recent advances in energy-saving chemiresistive gas sensors: a review, *Nano Energy*, 2021, **79**, 105369.

86 S. H. Hosseini-Shokouh, J. Zhou, E. Berger, Z.-P. Lv, X. Hong, V. Virtanen, K. Kordas and H.-P. Komsa, Highly selective H_2S gas sensor based on $Ti_3C_2T_x$ MXene–organic composites, *ACS Appl. Mater. Interfaces*, 2023, **15**, 7063–7073.

87 Z. Shahrbabaki, S. Farajikhah, M. B. Ghasemian, F. Oveissi, R. J. Rath, J. Yun, F. Dehghani and S. Naficy, A flexible and polymer-based chemiresistive CO_2 gas sensor at room temperature, *Adv. Mater. Technol.*, 2023, **8**, 2201510.

88 H. Yuan, J. Tao, N. Li, A. Karmakar, C. Tang, H. Cai, S. J. Pennycook, N. Singh and D. Zhao, On-chip tailorability of capacitive gas sensors integrated with metal–organic framework films, *Angew. Chem., Int. Ed.*, 2019, **58**, 14089–14094.

89 H. Tang, L. N. Sacco, S. Vollebregt, H. Ye, X. Fan and G. Zhang, Recent advances in 2D/nanostructured metal sulfide-based gas sensors: mechanisms, applications, and perspectives, *J. Mater. Chem. A*, 2020, **8**, 24943–24976.

90 J. Li, Y. J. Lu, Q. Ye, M. Cinke, J. Han and M. Meyyappan, Carbon nanotube sensors for gas and organic vapor detection, *Nano Lett.*, 2003, **3**, 929–933.

91 Z. Zou, Z. Zhao, Z. Zhang, W. Tian, C. Yang, X. Jin and K. Zhang, Room-temperature optoelectronic gas sensor based on core–shell g-C_3N_4@WO_3 heterocomposites for efficient ammonia detection, *Anal. Chem.*, 2023, **95**, 2110–2118.

92 A. K. Elger and C. Hess, Elucidating the mechanism of working SnO_2 gas sensors using combined operando UV/Vis, Raman, and IR spectroscopy, *Angew. Chem., Int. Ed.*, 2019, **58**, 15057–15061.

93 D. Degler, U. Weimar and N. Barsan, Current understanding of the fundamental mechanisms of doped and loaded semiconducting metal-oxide-based gas sensing materials, *ACS Sens.*, 2019, **4**, 2228–2249.

94 S. Zhou, Q. Lu, M. Chen, B. Li, H. Wei, B. Zi, J. Zeng, Y. Zhang, J. Zhang, Z. Zhu and Q. Liu, Platinum-supported cerium-doped indium oxide for highly sensitive triethylamine gas sensing with good antihumidity, *ACS Appl. Mater. Interfaces*, 2020, **12**, 42962–42970.

95 Y. Xu, W. Zheng, X. Liu, L. Zhang, L. Zheng, C. Yang, N. Pinna and J. Zhang, Platinum single atoms on tin oxide ultrathin films for extremely sensitive gas detection, *Mater. Horiz.*, 2020, **7**, 1519–1527.

96 D. Li, Y. Li, X. Wang, G. Sun, J. Cao and Y. Wang, Surface modification of In_2O_3 porous nanospheres with Au single atoms for ultrafast and highly sensitive detection of CO, *Appl. Surf. Sci.*, 2023, **613**, 155987.

97 P. Wang, S. Guo, Z. Hu, L. Zhou, T. Li, S. Pu, H. Mao, H. Cai, Z. Zhu, B. Chen, H. Y. Li and H. Liu, Single-atom Cu stabilized on ultrathin $WO_{2.72}$ nanowire for highly

selective and ultrasensitive ppb-level toluene detection, *Adv. Sci.*, 2023, **10**, e2302778.

98 J. Hu, S. Zhai, Q. Zhang, H. Cui and X. Jiang, Two-dimensional $HfTe_2$ monolayer treated by dispersed single Pt atom for hazardous gas Detection: A First-principles study, *Appl. Surf. Sci.*, 2022, **605**, 154572.

99 L. Mu, D. Chen and H. Cui, Single Pd atom embedded Janus HfSeTe as promising sensor for dissolved gas detection in transformer oil: A density functional theory study, *Surf. Interfaces*, 2022, **35**, 102398.

100 A. Chen, Y. Han, Z. Wang, J. Cai, S. Ye and J. Li, Single atom modified two-dimensional bismuthenes for toxic gas detection, *Phys. Chem. Chem. Phys.*, 2023, **25**, 9249–9255.

101 Q. Rong, B. Xiao, J. Zeng, R. Yu, B. Zi, G. Zhang, Z. Zhu, J. Zhang, J. Wu and Q. Liu, Pt single atom-induced activation energy and adsorption enhancement for an ultrasensitive ppb-level methanol gas sensor, *ACS Sens.*, 2022, **7**, 199–206.

102 Q. Zhou, L. Yang, Z. Kan, J. Lyu, M. Xuan Wang, B. Dong, X. Bai, Z. Chang, H. Song and L. Xu, Diverse scenarios selective perception of H_2S via cobalt sensitized MOF filter membrane coated three-dimensional metal oxide sensor, *Chem. Eng. J.*, 2022, **450**, 138014.

103 V. V. Ganbavle, S. I. Inamdar, G. L. Agawane, J. H. Kim and K. Y. Rajpure, Synthesis of fast response, highly sensitive and selective Ni:ZnO based NO_2 sensor, *Chem. Eng. J.*, 2016, **286**, 36–47.

104 Y. Zou, S. Chen, J. Sun, J. Liu, Y. Che, X. Liu, J. Zhang and D. Yang, Highly efficient gas sensor using a hollow SnO_2 microfiber for triethylamine detection, *ACS Sens.*, 2017, **2**, 897–902.

105 W. Yang, P. Wan, M. Jia, J. Hu, Y. Guan and L. Feng, A novel electronic nose based on porous In_2O_3 microtubes sensor array for the discrimination of VOCs, *Biosens. Bioelectron.*, 2015, **64**, 547–553.

106 B. Zong, Q. Xu and S. Mao, Single-atom Pt-functionalized $Ti_3C_2T_x$ field-effect transistor for volatile organic compound gas detection, *ACS Sens.*, 2022, **7**, 1874–1882.

107 B. Liu, L. Zhang, Y. Luo, L. Gao and G. Duan, The dehydrogenation of H-S bond into sulfur species on supported Pd single atoms allows highly selective and sensitive hydrogen sulfide detection, *Small*, 2021, **17**, e2105643.

108 L. Zhou, X. Chang, W. Zheng, X. Liu and J. Zhang, Single atom Rh-sensitized SnO_2 via atomic layer deposition for efficient formaldehyde detection, *Chem. Eng. J.*, 2023, **475**, 146300.

109 T. Yuan, Z. Xue, Y. Chen and J. Xu, Single Pt atom-based gas sensor: Break the detection limit and selectivity of acetone, *Sens. Actuators, B*, 2023, **397**, 134139.

110 B. Liu, Q. Zhu, Y. Pan, F. Huang, L. Tang, C. Liu, Z. Cheng, P. Wang, J. Ma and M. Ding, Single-atom tailoring of two-dimensional atomic crystals enables highly efficient detection and pattern recognition of chemical vapors, *ACS Sens.*, 2022, **7**, 1533–1543.

111 L. Liu, C. Mao, H. Fu, X. Qu and S. Zheng, ZnO nanorod-immobilized Pt single-atoms as an ultrasensitive sensor for triethylamine detection, *ACS Appl. Mater. Interfaces*, 2023, **15**, 16654–16663.

112 Y.-Z. Liu, R.-T. Guo, C.-P. Duan, G.-L. Wu, Y.-F. Miao, J.-W. Gu and W.-G. Pan, Removal of gaseous pollutants by using 3DOM-based catalysts: A review, *Chemosphere*, 2021, **262**, 127886.

113 J. Xiang, Y. Su, L. Zhang, S. Hong, Z. Wang, D. Han and F. Gu, Atomically dispersed Pt on three-dimensional ordered macroporous SnO_2 for highly sensitive and highly selective detection of triethylamine at a low working temperature, *ACS Appl. Mater. Interfaces*, 2022, **14**, 13440–13449.

114 F. Gu, Y. Cui, D. Han, S. Hong, M. Flytzani-Stephanopoulos and Z. Wang, Atomically dispersed Pt (II) on WO_3 for highly selective sensing and catalytic oxidation of triethylamine, *Appl. Catal., B*, 2019, **256**, 117809.

115 X.-L. Ye, S.-J. Lin, J.-W. Zhang, H.-J. Jiang, L.-A. Cao, Y.-Y. Wen, M.-S. Yao, W.-H. Li, G.-E. Wang and G. Xu, Boosting room temperature sensing performances by atomically dispersed Pd stabilized via surface coordination, *ACS Sens.*, 2021, **6**, 1103–1110.

116 R. Lang, X. Du, Y. Huang, X. Jiang, Q. Zhang, Y. Guo, K. Liu, B. Qiao, A. Wang and T. Zhang, Single-atom catalysts based on the metal–oxide interaction, *Chem. Rev.*, 2020, **120**, 11986–12043.

117 N. Murata, T. Suzuki, Y. Lin, H. Nitani, Y. Niwa, T. Wada, M. Uo and K. Asakura, Structure of atomically dispersed Pt in a SnO_2 thin film under reaction conditions: origin of its high performance in micro electromechanical system gas sensor catalysis, *ACS Appl. Mater. Interfaces*, 2022, **14**, 39507–39514.

118 J. Liu, Y. Tang, Y. Wang, T. Zhang and J. Li, Theoretical understanding of the stability of single-atom catalysts, *Natl. Sci. Rev.*, 2018, **5**, 638–641.

119 R. Qin, P. Liu, G. Fu and N. Zheng, Strategies for stabilizing atomically dispersed metal catalysts, *Small Methods*, 2018, **2**, 1700286.

120 T. Dai, Z. Yan, M. Li, Y. Han, Z. Deng, S. Wang, R. Wang, X. Xu, L. Shi, W. Tong, J. Bao, Z. Qiao, L. Li and G. Meng, Boosting electrical response toward trace volatile organic compounds molecules via pulsed temperature modulation of Pt anchored WO_3 chemiresistor, *Small Methods*, 2022, **6**, e2200728.

121 L. Li, H. Su, L. Zhou, Z. Hu, T. Li, B. Chen, H.-Y. Li and H. Liu, Single-atom Ce targeted regulation SnS/SnS_2 heterojunction for sensitive and stable room-temperature ppb-level gas sensor, *Chem. Eng. J.*, 2023, **472**, 144796.

122 S. Zhai, X. Jiang, D. Wu, L. Chen, Y. Su, H. Cui and F. Wu, Single Rh atom decorated pristine and S-defected PdS_2 monolayer for sensing thermal runaway gases in a lithium-ion battery: A first-principles study, *Surf. Interfaces*, 2023, **37**, 102735.

123 K. Koga, Electronic and catalytic effects of single-atom Pd additives on the hydrogen sensing properties of Co_3O_4 nanoparticle films, *ACS Appl. Mater. Interfaces*, 2020, **12**, 20806–20823.

124 B. Liu, K. Li, Y. Luo, L. Gao and G. Duan, Sulfur spillover driven by charge transfer between AuPd alloys and SnO_2 allows high selectivity for dimethyl disulfide gas sensing, *Chem. Eng. J.*, 2021, **420**, 129881.

125 Q. Zhou, W. Zeng, W. Chen, L. Xu, R. Kumar and A. Umar, High sensitive and low-concentration sulfur dioxide (SO_2) gas sensor application of heterostructure NiO-ZnO nanodisks, *Sens. Actuators, B*, 2019, **298**, 126870.

126 T. Wang, J. Hao, S. Zheng, Q. Sun, D. Zhang and Y. Wang, Highly sensitive and rapidly responding room-temperature NO_2 gas sensors based on WO_3 nanorods/sulfonated graphene nanocomposites, *Nano Res.*, 2018, **11**, 791–803.

127 H. Shin, W.-G. Jung, D.-H. Kim, J.-S. Jang, Y. H. Kim, W.-T. Koo, J. Bae, C. Park, S.-H. Cho, B. J. Kim and I.-D. Kim, Single-atom Pt stabilized on one-dimensional nanostructure support via carbon nitride/SnO_2 heterojunction trapping, *ACS Nano*, 2020, **14**, 11394–11405.

128 L. Sun, B. Wang and Y. Wang, High-temperature gas sensor based on novel Pt single atoms@SnO_2 nanorods@SiC nanosheets multi-heterojunctions, *ACS Appl. Mater. Interfaces*, 2020, **12**, 21808–21817.

129 R. Tian, S. Wang, X. Hu, J.-G. Zheng, P. Ji, J. Lin, J. Zhang, M. Xu, J. Bao, S. Zuo, H. Zhang, W. Zhang, J. Wang and L. Yu, Novel approaches for highly selective, room-temperature gas sensors based on atomically dispersed non-precious metals, *J. Mater. Chem. A*, 2020, **8**, 23784–23794.

130 J. Ding, H. Yang, X.-L. Ma, S. Liu, W. Liu, Q. Mao, Y. Huang, J. Li, T. Zhang and B. Liu, A tin-based tandem electrocatalyst for CO_2 reduction to ethanol with 80% selectivity, *Nat. Energy*, 2023, **8**, 1386–1394.

131 X. Geng, S. Li, L. Mawella-Vithanage, T. Ma, M. Kilani, B. Wang, L. Ma, C. C. Hewa-Rahinduwage, A. Shafikova, E. Nikolla, G. Mao, S. L. Brock, L. Zhang and L. Luo, Atomically dispersed Pb ionic sites in PbCdSe quantum dot gels enhance room-temperature NO_2 sensing, *Nat. Commun.*, 2021, **12**, 4895.

132 Z. G. Xue, M. Y. Yan, X. Yu, Y. J. Tong, H. Zhou, Y. F. Zhao, Z. Y. Wang, Y. S. Zhang, C. Xiong, J. Yang, X. Hong, J. Luo, Y. Lin, W. X. Huang, Y. Li and Y. E. Wu, One-dimensional segregated single Au sites on step-rich ZnO ladder for ultrasensitive NO_2 sensors, *Chem*, 2020, **6**, 3364–3373.

133 G. Li, H. Zhang, L. Meng, Z. Sun, Z. Chen, X. Huang and Y. Qin, Adjustment of oxygen vacancy states in ZnO and its application in ppb-level NO_2 gas sensor, *Sci. Bull.*, 2020, **65**, 1650–1658.

134 S. Zhao, Y. Yang, F. Bi, Y. Chen, M. Wu, X. Zhang and G. Wang, Oxygen vacancies in the catalyst: Efficient degradation of gaseous pollutants, *Chem. Eng. J.*, 2023, **454**, 140376.

135 L. Liu, P. Zhou, X. Su, Y. Liu, Y. Sun, H. Yang, H. Fu, X. Qu, S. Liu and S. Zheng, Synergistic Ni single atoms and oxygen vacancies on SnO_2 nanorods toward promoting SO_2 gas sensing, *Sens. Actuators, B*, 2022, **351**, 130983.

136 Z. Zhao, P. Zhang, H. Tan, X. Liang, T. Li, Y. Gao and C. Hu, Low concentration of peroxymonosulfate triggers dissolved oxygen conversion over single atomic Fe–N_3O_1 sites for water decontamination, *Small*, 2023, **19**, 2205583.

137 B. Huang, Z. Wu, H. Zhou, J. Li, C. Zhou, Z. Xiong, Z. Pan, G. Yao and B. Lai, Recent advances in single-atom catalysts for advanced oxidation processes in water purification, *J. Hazard. Mater.*, 2021, **412**, 125253.

138 W. Ma, M. Sun, D. Huang, C. Chu, T. Hedtke, X. Wang, Y. Zhao, J.-H. Kim and M. Elimelech, Catalytic membrane with copper single-atom catalysts for effective hydrogen peroxide activation and pollutant destruction, *Environ. Sci. Technol.*, 2022, **56**, 8733–8745.

139 Y. Liu, L. Liu and Y. Wang, A critical review on removal of gaseous pollutants using sulfate radical-based advanced oxidation technologies, *Environ. Sci. Technol.*, 2021, **55**, 9691–9710.

140 Z. Wan, X. Hu, C. Li, J. Zhang, Q. Wang, L. Fang, L. Zhang, Q. Guo and D. Sun, Simultaneous oxidation and absorption of nitric oxide and sulfur dioxide by peroxymonosulfate activated by bimetallic metal-organic frameworks, *J. Environ. Chem. Eng.*, 2023, **11**, 109417.

141 M. S. Johnson, E. J. K. Nilsson, E. A. Svensson and S. Langer, Gas-phase advanced oxidation for effective, efficient in situ control of pollution, *Environ. Sci. Technol.*, 2014, **48**, 8768–8776.

142 Z. Chen, J. Li, S. Wang, J. Zhao, J. Liu, J. Shen, C. Qi and P. Yang, Structure-property-performance relationship of transition metal doped WO3 mixed oxides for catalytic degradation of organic pollutants, *Chemosphere*, 2023, **316**, 137797.

143 B. Lin, Z. Guo, J. Li, G. Xiao, D. Ye and Y. Hu, V-Cu bimetallic oxide supported catalysts for synergistic removal of toluene and NO_x from coal-fired flue gas: The crucial role of support, *Chem. Eng. J.*, 2023, **458**, 141443.

144 Z. Zhang, Y. Zhu, H. Asakura, B. Zhang, J. Zhang, M. Zhou, Y. Han, T. Tanaka, A. Wang, T. Zhang and N. Yan, Thermally stable single atom Pt/m-Al_2O_3 for selective hydrogenation and CO oxidation, *Nat. Commun.*, 2017, **8**, 16100.

145 S. Wang and J. Wang, Single atom cobalt catalyst derived from co-pyrolysis of vitamin B_{12} and graphitic carbon nitride for PMS activation to degrade emerging pollutants, *Appl. Catal., B*, 2023, **321**, 122051.

146 J. Xu, Y. Wang, K. Wang, M. Zhao, R. Zhang, W. Cui, L. Liu, M. S. Bootharaju, J. H. Kim, T. Hyeon, H. Zhang, Y. Wang, S. Song and X. Wang, Single-atom Rh on high-index CeO_2 facet for highly enhanced catalytic CO oxidation, *Angew. Chem., Int. Ed.*, 2023, **62**, e202302877.

147 M. Mahmoodinia, P.-O. Åstrand and D. Chen, Tuning the electronic properties of single-atom Pt catalysts by functionalization of the carbon support material, *J. Phys. Chem. C*, 2017, **121**, 20802–20812.

148 B.-T. Qiao, J.-X. Liang, A.-Q. Wang, J.-Y. Liu and T. Zhang, Single atom gold catalysts for low-temperature CO oxidation, *Chin. J. Catal.*, 2016, **37**, 1580–1586.

149 R. Shan, Z. Sheng, S. Hu, H. Xiao, Y. Zhang, J. Zhang, L. Wang, C. Zhang and J. Li, Enhancing oxidation

reaction over Pt-MnO_2 catalyst by activation of surface oxygen, *J. Environ. Sci.*, 2023, **134**, 117–125.

150 J. Liu, X. Fang, D. Liu, X. Hu, T. Qin, J. Chen, R. Liu, D. Xu, W. Qu, Y. Dong, L. Chen, Z. Ma, X. Liu, X. Li and X. Tang, Benzene abatement catalyzed by Ceria-Supported platinum nanoparticles and single atoms, *Chem. Eng. J.*, 2023, **467**, 143407.

151 Y. Chen, Z. Huang, M. Zhou, Z. Ma, J. Chen and X. Tang, Single silver adatoms on nanostructured manganese oxide surfaces: Boosting oxygen activation for benzene abatement, *Environ. Sci. Technol.*, 2017, **51**, 2304–2311.

152 H. Deng, S. Kang, J. Ma, C. Zhang and H. He, Silver incorporated into cryptomelane-type Manganese oxide boosts the catalytic oxidation of benzene, *Appl. Catal., B*, 2018, **239**, 214–222.

153 J. Chen, D. Yan, Z. Xu, X. Chen, X. Chen, W. Xu, H. Jia and J. Chen, A novel redox precipitation to synthesize Au-doped α-MnO_2 with high dispersion toward low-temperature oxidation of formaldehyde, *Environ. Sci. Technol.*, 2018, **52**, 4728–4737.

154 J. Chen, M. Jiang, J. Chen, W. Xu and H. Jia, Selective immobilization of single-atom Au on cerium dioxide for low-temperature removal of C1 gaseous contaminants, *J. Hazard. Mater.*, 2020, **392**, 122511.

155 H. Zhang, S. Sui, X. Zheng, R. Cao and P. Zhang, One-pot synthesis of atomically dispersed Pt on MnO_2 for efficient catalytic decomposition of toluene at low temperatures, *Appl. Catal., B*, 2019, **257**, 117878.

156 J. Chen, M. Jiang, W. Xu, J. Chen, Z. Hong and H. Jia, Incorporating Mn cation as anchor to atomically disperse Pt on TiO_2 for low-temperature removal of formaldehyde, *Appl. Catal., B*, 2019, **259**, 118013.

157 G. Liu, J. Zhou, W. Zhao, Z. Ao and T. An, Single atom catalytic oxidation mechanism of formaldehyde on Al doped graphene at room temperature, *Chin. Chem. Lett.*, 2020, **31**, 1966–1969.

158 Z. Hou, L. Dai, Y. Liu, J. Deng, L. Jing, W. Pei, R. Gao, Y. Feng and H. Dai, Highly efficient and enhanced sulfur resistance supported bimetallic single-atom palladium–cobalt catalysts for benzene oxidation, *Appl. Catal., B*, 2021, **285**, 119844.

159 J. K. Lampert, M. S. Kazi and R. J. Farrauto, Palladium catalyst performance for methane emissions abatement from lean burn natural gas vehicles, *Appl. Catal., B*, 1997, **14**, 211–223.

160 C. Gao, J. Low, R. Long, T. Kong, J. Zhu and Y. Xiong, Heterogeneous single-atom photocatalysts: fundamentals and applications, *Chem. Rev.*, 2020, **120**, 12175–12216.

161 J. Qin, Y. Pei, Y. Zheng, D. Ye and Y. Hu, Fe-MOF derivative photocatalyst with advanced oxygen reduction capacity for indoor pollutants removal, *Appl. Catal., B*, 2023, **325**, 122346.

162 S. Zhao, H. Choe, S. Saqlain, C.-C. Hwang, Z. Liu, Y. Choi, Z. Peng and Y. D. Kim, Simultaneous oxidation of NO and acetaldehyde over bare and Fe-modified TiO_2 under visible light irradiation, *Appl. Surf. Sci.*, 2023, **627**, 157308.

163 J. Ding, Z. Teng, X. Su, K. Kato, Y. Liu, T. Xiao, W. Liu, L. Liu, Q. Zhang, X. Ren, J. Zhang, Z. Chen, O. Teruhisa, A. Yamakata, H. Yang, Y. Huang, B. Liu and Y. Zhai, Asymmetrically coordinated cobalt single atom on carbon nitride for highly selective photocatalytic oxidation of CH_4 to CH_3OH, *Chem*, 2023, **9**, 1017–1035.

164 X. Wu, H. Zhang, J. Dong, M. Qiu, J. Kong, Y. Zhang, Y. Li, G. Xu, J. Zhang and J. Ye, Surface step decoration of isolated atom as electron pumping: Atomic-level insights into visible-light hydrogen evolution, *Nano Energy*, 2018, **45**, 109–117.

165 B.-H. Lee, S. Park, M. Kim, A. K. Sinha, S. C. Lee, E. Jung, W. J. Chang, K.-S. Lee, J. H. Kim, S.-P. Cho, H. Kim, K. T. Nam and T. Hyeon, Reversible and cooperative photoactivation of single-atom Cu/TiO_2 photocatalysts, *Nat. Mater.*, 2019, **18**, 620–626.

166 X. Li, Z. Le, X. Chen, Z. Li, W. Wang, X. Liu, A. Wu, P. Xu and D. Zhang, Graphene oxide enhanced amine-functionalized titanium metal organic framework for visible-light-driven photocatalytic oxidation of gaseous pollutants, *Appl. Catal., B*, 2018, **236**, 501–508.

167 M. Wen, G. Li, H. Liu, J. Chen, T. An and H. Yamashita, Metal–organic framework-based nanomaterials for adsorption and photocatalytic degradation of gaseous pollutants: recent progress and challenges, *Environ. Sci.: Nano*, 2019, **6**, 1006–1025.

168 L. Luo, J. Luo, H. Li, F. Ren, Y. Zhang, A. Liu, W.-X. Li and J. Zeng, Water enables mild oxidation of methane to methanol on gold single-atom catalysts, *Nat. Commun.*, 2021, **12**, 1218.

169 Z.-H. Xue, D. Luan, H. Zhang and X. W. Lou, Single-atom catalysts for photocatalytic energy conversion, *Joule*, 2022, **6**, 92–133.

170 X.-L. Wu, S. Liu, Y. Li, M. Yan, H. Lin, J. Chen, S. Liu, S. Wang and X. Duan, Directional and Ultrafast Charge Transfer in Oxygen-Vacancy-Rich ZnO@Single-Atom Cobalt Core-Shell Junction for Photo-Fenton-Like Reaction, *Angew. Chem., Int. Ed.*, 2023, **62**, e202305639.

171 Y. Zou, J. Hu, B. Li, L. Lin, Y. Li, F. Liu and X.-y. Li, Tailoring the coordination environment of cobalt in a single-atom catalyst through phosphorus doping for enhanced activation of peroxymonosulfate and thus efficient degradation of sulfadiazine, *Appl. Catal., B*, 2022, **312**, 121408.

172 D. Li, S. Zhang, S. Li, J. Tang, T. Hua and F. Li, Mechanism of the application of single-atom catalyst-activated PMS/PDS to the degradation of organic pollutants in water environment: A review, *J. Cleaner Prod.*, 2023, **397**, 136468.

173 Z. Wang, S. Xie, Y. Feng, P. Ma, K. Zheng, E. Duan, Y. Liu, H. Dai and J. Deng, Simulated solar light driven photothermal catalytic purification of toluene over iron oxide supported single atom Pt catalyst, *Appl. Catal., B*, 2021, **298**, 120612.

174 Y. Feng, L. Dai, Z. Wang, Y. Peng, E. Duan, Y. Liu, L. Jing, X. Wang, A. Rastegarpanah, H. Dai and J. Deng, Photothermal synergistic effect of Pt_1/CuO-CeO_2 single-

atom catalysts significantly improving toluene removal, *Environ. Sci. Technol.*, 2022, **56**, 8722–8732.

175 E. Agbovhimen Elimian, M. Zhang, Y. Sun, J. He and H. Jia, Harnessing solar energy towards synergistic photothermal catalytic oxidation of volatile organic compounds, *Sol. RRL*, 2023, **7**, 2300238.

176 K. Li, W. Cui, J. Li, Y. Sun, Y. Chu, G. Jiang, Y. Zhou, Y. Zhang and F. Dong, Tuning the reaction pathway of photocatalytic NO oxidation process to control the secondary pollution on monodisperse Au nanoparticles@g-C_3N_4, *Chem. Eng. J.*, 2019, **378**, 122184.

177 Z. Teng, Q. Zhang, H. Yang, K. Kato, W. Yang, Y.-R. Lu, S. Liu, C. Wang, A. Yamakata, C. Su, B. Liu and T. Ohno, Atomically dispersed antimony on carbon nitride for the artificial photosynthesis of hydrogen peroxide, *Nat. Catal.*, 2021, **4**, 374–384.

178 R. Zhang, Y. Cao, D. E. Doronkin, M. Ma, F. Dong and Y. Zhou, Single-atom dispersed Zn-N_3 active sites bridging the interlayer of g-C_3N_4 to tune NO oxidation pathway for the inhibition of toxic by-product generation, *Chem. Eng. J.*, 2023, **454**, 140084.

179 X. Wu, S. Sun, R. Wang, Z. Huang, H. Shen, H. Zhao and G. Jing, Pt single atoms and defect engineering of TiO_2-nanosheet-assembled hierarchical spheres for efficient room-temperature HCHO oxidation, *J. Hazard. Mater.*, 2023, **454**, 131434.

180 J. Chen, L. Chen, X. Wang, J. Sun, A. Chen and X. Xie, Er single atoms decorated TiO_2 and Er^{3+} ions modified TiO_2 for photocatalytic oxidation of mixed VOCs, *Appl. Surf. Sci.*, 2022, **596**, 153655.

181 K. Mori, T. Murakami and H. Yamashita, Luminescent single-atom Eu-coordinated graphitic carbon nitride nanosheets for selective sensing of acetone and cyclohexane, *ACS Appl. Nano Mater.*, 2020, **3**, 10209–10217.

182 D. Xia, W. Xu, Y. Wang, J. Yang, Y. Huang, L. Hu, C. He, D. Shu, D. Y. C. Leung and Z. Pang, Enhanced performance and conversion pathway for catalytic ozonation of methyl mercaptan on single-atom Ag deposited three-dimensional ordered mesoporous MnO_2, *Environ. Sci. Technol.*, 2018, **52**, 13399–13409.

183 Z. Hu, X. Li, S. Zhang, Q. Li, J. Fan, X. Qu and K. Lv, Fe_1/TiO_2 hollow microspheres: Fe and Ti dual active sites boosting the photocatalytic oxidation of NO, *Small*, 2020, **16**, e2004583.

184 G. Liu, Y. Huang, H. Lv, H. Wang, Y. Zeng, M. Yuan, Q. Meng and C. Wang, Confining single-atom Pd on g-C_3N_4 with carbon vacancies towards enhanced photocatalytic NO conversion, *Appl. Catal., B*, 2021, **284**, 119683.

185 Y. Liu, S. Shi and Y. Wang, Removal of pollutants from gas streams using Fenton (-like)-based oxidation systems: A review, *J. Hazard. Mater.*, 2021, **416**, 125927.

186 S. Liu, Y. Hu, H. Xu, Z. Lou, J. Chen, C.-Z. Yuan, X. Lv, X. Duan, S. Wang and X.-L. Wu, Directional electron transfer in single-atom cobalt nanozyme for enhanced photo-Fenton-like reaction, *Appl. Catal., B*, 2023, **335**, 122882.

187 S. Liu, D. Liu, Y. Sun, P. Xiao, H. Lin, J. Chen, X.-L. Wu, X. Duan and S. Wang, Enzyme-mimicking single-atom FeN_4 sites for enhanced photo-Fenton-like reactions, *Appl. Catal., B*, 2022, **310**, 121327.

188 L. Mu, M. Wang, F. Jiang, Q. Gao, M. Zhang, Z. Xiong, Y. Li, R. Shen, J. Hu and G. Wu, Boosting Photo-Fenton reactions by amidoxime chelated ferrous iron (Fe(III)) catalyst for highly efficient pollutant control, *Appl. Catal., B*, 2021, **298**, 120574.

189 H. Yang, Y. Wu, X. Zheng, S. Wu, B. Zhang, L. Hu, X. Guo and B. Wu, A review on gaseous pollutants purification using H_2O_2-based Fenton-like reactions, *J. Environ. Chem. Eng.*, 2023, **11**, 111066.

190 L. Su, P. Wang, X. Ma, J. Wang and S. Zhan, Regulating local electron density of iron single sites by introducing nitrogen vacancies for efficient photo-Fenton process, *Angew. Chem., Int. Ed.*, 2021, **60**, 21261–21266.

191 F. Chen, X.-L. Wu, C. Shi, H. Lin, J. Chen, Y. Shi, S. Wang and X. Duan, Molecular engineering toward pyrrolic N-rich M-N_4 (M = Cr, Mn, Fe, Co, Cu) single-atom sites for enhanced heterogeneous Fenton-like reaction, *Adv. Funct. Mater.*, 2021, **31**, 2007877.

192 H. Song, L. Wei, C. Chen, C. Wen and F. Han, Photocatalytic production of H_2O_2 and its *in situ* utilization over atomic-scale Au modified MoS_2 nanosheets, *J. Catal.*, 2019, **376**, 198–208.

193 Y. Zhou, M. Yu, Q. Zhang, X. Sun and J. Niu, Regulating electron distribution of Fe/Ni-N_4P_2 single sites for efficient photo-Fenton process, *J. Hazard. Mater.*, 2022, **440**, 129724.

194 Z. Zhao, W. Zhang, W. Liu, Y. Li, J. Ye, J. Liang and M. Tong, Activation of sulfite by single-atom Fe deposited graphitic carbon nitride for diclofenac removal: The synergetic effect of transition metal and photocatalysis, *Chem. Eng. J.*, 2021, **407**, 127167.

195 X. Li, X. Huang, S. Xi, S. Miao, J. Ding, W. Cai, S. Liu, X. Yang, H. Yang, J. Gao, J. Wang, Y. Huang, T. Zhang and B. Liu, Single cobalt atoms anchored on porous N-doped graphene with dual reaction sites for efficient Fenton-like catalysis, *J. Am. Chem. Soc.*, 2018, **140**, 12469–12475.

196 H. Tang, B. Ma, Z. Bian and H. Wang, Selective dechlorination degradation of chlorobenzenes by dual single-atomic Fe/Ni catalyst with M-N/M-O active sites synergistic, *J. Hazard. Mater.*, 2023, **443**, 130315.

197 S. Liu, G. Xing and J.-y. Liu, Computational screening of single-atom catalysts for direct electrochemical NH_3 synthesis from NO on defective boron phosphide monolayer, *Appl. Surf. Sci.*, 2023, **611**, 155764.

198 H. Yin, Y. Peng and J. Li, Electrocatalytic Reduction of Nitrate to Ammonia via a Au/Cu Single Atom Alloy Catalyst, *Environ. Sci. Technol.*, 2023, **57**, 3134–3144.

199 K. Chen, G. Wang, Y. Guo, D. Ma and K. Chu, Iridium single-atom catalyst for highly efficient NO electroreduction to NH_3, *Nano Res.*, 2023, **16**, 8737–8742.

200 L. Liu and S. Zheng, Advancements in single atom catalysts for electrocatalytic nitrate reduction reaction, *ChemCatChem*, 2024, e202301641.
201 D. Wang, X. Zhu, X. Tu, X. Zhang, C. Chen, X. Wei, Y. Li and S. Wang, Oxygen-bridged copper-iron atomic pair as dual-metal active sites for boosting electrocatalytic NO reduction, *Adv. Mater.*, 2023, **35**, e2304646.
202 Z. Wang, J. Zhao, J. Wang, C. R. Cabrera and Z. Chen, A Co–N_4 moiety embedded into graphene as an efficient single-atom-catalyst for NO electrochemical reduction: a computational study, *J. Mater. Chem. A*, 2018, **6**, 7547–7556.
203 B. Hammer and J. K. Norskov, Why gold is the noblest of all the metals, *Nature*, 1995, **376**, 238–240.
204 J. Greeley, J. K. Nørskov and M. Mavrikakis, Electronic structure and catalysis on metal surfaces, *Annu. Rev. Phys. Chem.*, 2002, **53**, 319–348.
205 K. Chen, J. Wang, H. Zhang, D. Ma and K. Chu, Self-tandem electrocatalytic NO reduction to NH_3 on a W single-atom catalyst, *Nano Lett.*, 2023, **23**, 1735–1742.
206 B. He, P. Lv, D. Wu, X. Li, R. Zhu, K. Chu, D. Ma and Y. Jia, Confinement catalysis of a single atomic vacancy assisted by aliovalent ion doping enabled efficient NO electroreduction to NH_3, *J. Mater. Chem. A*, 2022, **10**, 18690–18700.
207 K. Chen, N. Zhang, F. Wang, J. Kang and K. Chu, Main-group indium single-atom catalysts for electrocatalytic NO reduction to NH_3, *J. Mater. Chem. A*, 2023, **11**, 6814–6819.
208 Q. Song, M. Li, X. Hou, J. Li, Z. Dong, S. Zhang, L. Yang and X. Liu, Anchored Fe atoms for N=O bond activation to boost electrocatalytic nitrate reduction at low concentrations, *Appl. Catal., B*, 2022, **317**, 121721.
209 K. Chen, G. Zhang, X. Li, X. Zhao and K. Chu, Electrochemical NO reduction to NH_3 on Cu single atom catalyst, *Nano Res.*, 2022, **16**, 5857–5863.
210 M. Ran, H. Xu, Y. Bao, Y. Zhang, J. Zhang and M. Xing, Selective production of CO from organic pollutants by coupling piezocatalysis and advanced oxidation processes, *Angew. Chem., Int. Ed.*, 2023, **62**, e202303728.
211 Z. Chen, F. An, Y. Zhang, Z. Liang, W. Liu and M. Xing, Single-atom Mo–Co catalyst with low biotoxicity for sustainable degradation of high-ionization-potential organic pollutants, *Proc. Natl. Acad. Sci. U. S. A.*, 2023, **120**, e2305933120.
212 L. Jin, S. You, N. Ren, B. Ding and Y. Liu, Mo vacancy-mediated activation of peroxymonosulfate for ultrafast micropollutant removal using an electrified MXene filter functionalized with Fe single atoms, *Environ. Sci. Technol.*, 2022, **56**, 11750–11759.
213 L. Jin, S. You, Y. Yao, H. Chen, Y. Wang and Y. Liu, An electroactive single-atom copper anchored MXene nanohybrid filter for ultrafast water decontamination, *J. Mater. Chem. A*, 2021, **9**, 25964–25973.
214 C. Zhou, J. Li, Y. Zhang, J. Bai, P. Wang, B. Zhang, L. Zha, M. Long and B. Zhou, A novel $SO_3^{\bullet-}$ mediated photoelectrocatalytic system based on MoS_2/Fe_2O_3 and CuNW@CF for the efficient treatment of sulfurous and nitrogenous oxides, *Appl. Catal., B*, 2023, **330**, 122579.
215 S. Li, H. Shang, Y. Tao, P. Li, H. Pan, Q. Wang, S. Zhang, H. Jia, H. Zhang, J. Cao, B. Zhang, R. Zhang, G. Li, Y. Zhang, D. Zhang and H. Li, Hydroxyl radical-mediated efficient photoelectrocatalytic NO oxidation with simultaneous nitrate storage using a flow photoanode reactor, *Angew. Chem., Int. Ed.*, 2023, **62**, e202305538.
216 J.-J. Liu, S.-N. Sun, J. Liu, Y. Kuang, J.-W. Shi, L.-Z. Dong, N. Li, J.-N. Lu, J.-M. Lin, S.-L. Li and Y.-Q. Lan, Achieving high-efficient photoelectrocatalytic degradation of 4-chlorophenol via functional reformation of titanium-oxo clusters, *J. Am. Chem. Soc.*, 2023, **145**, 6112–6122.
217 J. Zhang, J. Sun, H. Zhao and G. Zhao, Single-atom copper promotes efficient generation of hydroxyl radicals under alkaline circumstances in a photoelectrochemical oxygen reduction process, *ACS EST Engg.*, 2022, **2**, 1953–1963.
218 J. Zhang, Z. Zhou, Z. Feng, H. Zhao and G. Zhao, Fast generation of hydroxyl radicals by rerouting the electron transfer pathway via constructed chemical channels during the photo-electro-reduction of oxygen, *Environ. Sci. Technol.*, 2022, **56**, 1331–1340.
219 J. Zhang, G. Zhang, H. Lan, H. Liu and J. Qu, Sustainable nitrogen fixation over Ru single atoms decorated Cu_2O using electrons produced from photoelectrocatalytic organics degradation, *Chem. Eng. J.*, 2022, **428**, 130373.
220 X. Li, H.-Y. Wang, H. Yang, W. Cai, S. Liu and B. Liu, In Situ/Operando Characterization Techniques to Probe the Electrochemical Reactions for Energy Conversion, *Small Methods*, 2018, **2**, 1700395.
221 J. Ding, F. Li, J. Zhang, Q. Zhang, Y. Liu, W. Wang, W. Liu, B. Wang, J. Cai, X. Su, H. B. Yang, X. Yang, Y. Huang, Y. Zhai and B. Liu, Circumventing CO_2 Reduction Scaling Relations Over the Heteronuclear Diatomic Catalytic Pair, *J. Am. Chem. Soc.*, 2023, **145**, 11829–11836.
222 S. Wei, Z. Li, K. Murugappan, Z. Li, F. Zhang, A. G. Saraswathyvilasam, M. Lysevych, H. H. Tan, C. Jagadish, A. Tricoli and L. Fu, A self-powered portable nanowire array gas sensor for dynamic NO_2 monitoring at room temperature, *Adv. Mater.*, 2023, **35**, 2207199.